

1
2
3
4
5
6
7
8
9
10
11
12
13
14
15
16
17
18
19
20
21
22
23
24
25
26
27

Title

Evidence from piezometer monitoring of *in situ* excess pore pressure and sediment deformation generated during the December 26, 2004 Great Sumatra-Andaman Earthquake

Authors

Nabil Sultan^{a*}, Antonio Cattaneo^a, Jean-Claude Sibuet^a, Jean-Luc Schneider^b and the «Sumatra Aftershocks» team#

Affiliations

^a Ifremer, Brest - GM, BP70, 29280 Plouzané, France

^b Université Bordeaux 1, OASU, CNRS-UMR 5805 “EPOC”, F-33405 Talence cedex, France

Keywords

Earthquake; Pore pressure; Slope failure; Sumatra; Tsunami

February 16, 2007

*Corresponding author
Nabil Sultan
Tel: +33 (0)2.98.22.42.59
Fax: +33 (0)2.98.22.45.70
E-mail: nabil.sultan@ifremer.fr

28 **ABSTRACT**

29 The swath bathymetric data acquired during the “Sumatra Aftershocks” cruise from the Sunda
30 trench in the Indian Ocean to the north of the Sumatra Island have shown the occurrence of
31 several scars and deposits corresponding to likely recent slope failures. *In situ* pore pressure
32 monitoring using the Ifremer piezometer and coring demonstrate that high excess pore
33 pressure and sediment deformation was generated by a recent event near a slope failure zone
34 identified by *J.T. Henstock* and co-authors. This excess pore pressure is localized in the upper
35 sedimentary layers and is not related to an interplate subduction process. Numerical
36 simulations of the hydrological system by taking into account the hydro-mechanical
37 properties of the upper sediment layer show that the excess pore pressure could be generated
38 at the time of the December 26, 2004 Great Sumatra Earthquake.

39 **INTRODUCTION**

40 The December 26, 2004 devastating Great Sumatra-Andaman Earthquake was the second
41 biggest earthquake ever recorded after the 1960 Chilean earthquake [*Stein and Okal, 2005*].
42 The earthquake was initiated close to the slab interface, at a depth of 20-30 km, in the vicinity
43 of an Indonesian fore-arc indentation. The rupture propagated 1300 km northwards from the
44 epicentral region located at 3.3°N, with an average propagation velocity of 2.1 km s⁻¹ [*Park et*
45 *al., 2005; Bilham et al., 2005; de Groot-Hedlin et al., 2004*]. For such a large earthquake,
46 aftershocks may last for several years and their location can be used to define the position of
47 the seismically active region.

48 The “Sumatra Aftershocks” cruise onboard the French R/V Marion Dufresne took place
49 during Summer 2005 (July, 14 - August, 9) to 1) record aftershocks and localize post-seismic
50 motions using Ocean Bottom Seismometers within a relatively short delay after the main
51 seismic event [*Sibuet et al., 2006 submitted*] and 2) enquire about submarine mass wasting
52 processes possibly associated with recent earthquakes. Even if the main trigger mechanism

53 for the tsunami appears to be linked to tectonic movements in the area of active convergence
54 between the Indo-Australian and the Southeast Asian plates [*Stein and Okal, 2005; Puspito,*
55 *2002*], the role of submarine slope instabilities and sediment failures in the tsunami initiation
56 remains unknown and deserves further investigation. A recent Special Issue of Marine
57 Geology [*Pelinovsky and Tinti, 2005*] summarized a series of case histories where the role of
58 mass wasting in the generation of tsunamis may have been either the main factor responsible
59 for the destructive wave (e.g. the 1929 Grand Banks tsunami; [*Fine et al., 2005*]) or could
60 have played a relevant role in amplifying the effect of earthquake-triggered tsunamis (e.g., in
61 the Marmara Sea [*Hébert et al., 2005*]).

62 In order to relate tectonic activities with seafloor failure features, swath bathymetric data
63 together with 3.5 kHz seismic profiles were acquired on a 40 x 200 nautical miles (74 x 370
64 km; ca. 27,000 km²) box oriented SW-NE between the India-Indonesian water limit and the
65 north-western tip of Sumatra Island [Figure 1– *Sibuet et al., 2006 submitted* and *Singh et al.,*
66 *2005*].

67 One of the main aims of this work is to enquire about the link between submarine mass
68 wasting processes and the most developed landslide identified by *Henstock et al. [2006]* along
69 the toe of the prism on one hand and the Great Sumatra Earthquake event on the other hand.
70 Therefore, in addition to the acquired bathymetric data, we carried out during the “Sumatra
71 Aftershocks” cruise heat flow measurements, sediment coring and *in situ* pore pressure
72 monitoring using the Ifremer piezometer.

73 **MATERIALS AND METHODS**

74 **Swath bathymetry and 3.5 kHz**

75 In order to investigate the sea-floor morphology, swath bathymetric mapping was conducted
76 during “Sumatra Aftershocks” 2005 cruise. Multibeam swath bathymetric data, together with
77 3.5 kHz seismic profiles, were acquired with a THALES Sea Falcon 11 integrated system.

78 The across-track resolution of the bathymetry depends upon the measured depth and is
79 typically equal to depth/100.

80 **Coring**

81 Twelve gravity and piston cores were recovered with *in situ* temperature measurements using
82 autonomous digital temperature probes fitted on gravity core barrels [see Sibuet et al., 2006,
83 submitted]. In the following, only three sediment cores and one *in situ* pore pressure
84 measurement from the HMS Scott landslide area are presented and discussed (Figure 2).

85 **Piezometer**

86 The study area is characterized by several submarine slope instability structures, but it is
87 difficult from the morphology alone to distinguish between sediment failures triggered by the
88 Great Sumatra Earthquake from older sediment failures. One of the key parameters for the
89 detection of co-seismic slope failures is the excess pore pressure within remolded sediment.
90 That is why the main aim of the use of the Ifremer piezometer in this project was to detect a
91 change of the pore pressure generated by the last major earthquakes events (December 2004
92 and March 2005). For this purpose, a piezometer was deployed to the North of the observed
93 mass wasting area (MD05-PZ1; see Figure 2 for location). The location of MD05-PZ1
94 coincides with that of core MD05-2975.

95 The Ifremer piezometer is a free-fall device similar to the Pop Up Pore Pressure Instrument
96 [Schultheiss and McPhail, 1986] with a sediment-piercing lance attached to a recoverable
97 instrument part. It is ballasted with lead weights to penetrate a range of sediment types in
98 water depths of up to 6000 m. The length of the used lance depends upon the stiffness of the
99 sediment. For soft sediment, a 12-metres lance can be used successfully. Pore pressures are
100 measured relative to hydrostatic pressure at maximum 5 ports on the 60 mm diameter lance
101 using specially adapted differential pressure transducers connected to the pressure ports and
102 the open sea-water. The piezometer pore pressure sensors have a resolution of ± 0.2 kPa

103 [Sultan *et al.*, 2007]. The Ifremer piezometer can be used in two modes: 1) long term
104 measurements where the equilibrium pore pressure can typically be reached after several days
105 (depending on the permeability of the medium and the depth of the sensor) and 2) short term
106 measurements where the equilibrium pressure is evaluated by plotting the pressure record
107 versus the reciprocal of time and extrapolated to $1/\text{time}=0$, a technique developed by *Davis et*
108 *al.* [1991] and *Fang et al.* [1993] and successfully used by *Urgeles et al.* [2000].

109 Figure 3 shows an example of pore pressure monitoring [from *Sultan et al.*, 2007] used to
110 validate the short-term piezometer measurements carried out during the “Sumatra
111 Aftershocks” cruise. Pore pressures were measured at two different levels (Figure 3-a:
112 11.6 mbsf and Figure 3-b: 10.1 mbsf). For the two sensors, the pore pressure equilibrium was
113 reached after around 2 days. The equilibrium pressure for the shallower sensor is found equal
114 to 9.5 kPa while it was equal to 11.2 kPa for the deeper sensor. The use of the *Davies et al.*
115 [1991] method after only 3.5 hours recording gave equilibrium pressures of 11 kPa at
116 11.6 mbsf and 10 kPa at 10.1 mbsf. The maximum error between the real equilibrium pore
117 pressures and extrapolated ones is acceptable and comparable to the precision of the pore
118 pressure sensors.

119 **RESULTS**

120 **Swath bathymetry**

121 Swath bathymetry data revealed several morphotectonic features. The study area (Figure 2) is
122 characterized by very steep slope angles reaching in some cases 30° . Several ridges are
123 collapsed and/or sliced by major or secondary faults [*Sibuet, 2005*]. A number of slope failure
124 scars and deposits were also identified in the whole investigated area presented in Figure 1
125 but no major and recent submarine landslide had been discovered yet.

126 The submarine landslide already identified by the British R/V HMS Scott at the frontal area
127 facing the Sumatra trench [*Henstock et al.*, 2006] is presented in Figure 2 with the bathymetry

128 acquired during the ‘Sumatra Aftershocks’ cruise. The slope failure occurs in water depths
129 ranging between 3300 and 4300 m. Figure 2 shows the presence of an eroded ridge to the
130 north of the HMS Scott landslide scarp. The western boundary of the eroded ridge is indicated
131 in Figure 4 (points A1 and E1). Figure 4 shows that the landslide is characterized by a series
132 of horseshoe-shaped headwall scars and sediment deposits with positive relief. Figure 5-a
133 shows three NE-SW cross sections across the northern part of the slope failure zone (A-A, B-
134 B and E-E). The boundary of the eroded ridge crest (arrows A1 and E1) and 5 landslide toes
135 (arrows A2, A3, B1, E2 and E3) already identified by *Henstock et al. [2006]* and
136 corresponding to several phases of failures are also indicated in Figure 5-a. Figure 5-a
137 displays two other NE-SW cross sections (C-C and D-D) across the 3 slides indicated in
138 Figure 4 showing again several scarps, which probably correspond to several phases of
139 failure. The slope angles determined along the C-C and E-E cross-sections are presented in
140 Figure 5-c and it indicates that along those two cross-sections, the maximum slope angle is
141 equal to 17 degrees. Several blocks and/or morphological bulges can be identified in Figure 2
142 and Figure 4 in the deep depositional area. The blocks and/or bulges are all comprised in an
143 area of about 10 x 8 km that is 1 to 10 km away from the base of the accretionary prism front.
144 Figure 6 shows three 3.5 kHz profiles acquired across the deposit area, the fracture zone and
145 the block field (for location see Figure 2). Figure 6-b shows the presence of 1) a lens-shaped
146 sediment accumulation with an irregular surface at the base of the accretionary prism front,
147 and 2) a sediment drape overlapping the small blocks. These two observations confirm the
148 existence of distinct sliding phases of different ages, since some blocks appear to represent
149 the expression of ancient events. To the Southwest of Core MD05-2981 (Figure 2-a), we
150 interpret the NE-SW oriented morphological step as the surface expression of a recent thrust
151 located within the sedimentary cover overlying the oceanic crust seaward of the toe of the

152 accretionary wedge. One of the arguments to prove the presence of such recent thrust is the
153 seafloor scarp about 20 ms high (ca. 15 m) clearly visible in Figure 6-c.

154 **Coring**

155 *Sedimentology*

156 Three cores were recovered from the HMS Scott landslide area (Figure 2, Figure 4 and Table
157 2). Two cores were acquired from the slope and one core in the trench basin at the base of the
158 slide. Core logging of physical properties (gamma density, P-wave velocity and magnetic
159 susceptibility) was conducted onboard on unopened 1.5-m-long core sections through a
160 GEOTEK core logging device (<http://www.geotek.co.uk/>). SCOPIX (X-ray) images were
161 obtained at the Bordeaux 1 University. Core description (including photo and X-ray images)
162 was not possible at depth where geotechnical samples were taken in cores MD05-2972 and
163 MD05-2975 because of the destructive nature of the geotechnical measurements.

164 Core MD05-2975 is a gravity core that recovered 5.72 m of sediment with a 12-m tube.
165 The core is located ca. 4 km upslope of slide scar 3 (to the north; Figure 4) at the same
166 location of piezometer MD05-PZ1. The sediment is composed by finely laminated silty clay
167 with traces of black organic matter in the upper 1.8 m (Figure 7-a). The upper 0.5 m shows
168 evidence for some bioturbation and higher water content. From 1.8 to 2.5 m bioturbation is
169 more visible and there are two levels richer in bioclast (mostly pteropods, Figure 7-b) that
170 could account for a slightly reduced unit weight at this level. The lithology is remarkably
171 homogeneous in the interval from 2.5 to 4 m (Figure 7-c and -d). X-ray image and, less
172 evidently, core photo, reveal an interval with presence of bioturbation and perturbation of
173 sedimentary structures especially from 4.4 to 4.8 m that we interpret as a possible evidence of
174 remolded sediment (Figure 7-e).

175 Core MD05-2972 is a 2.94-m long gravity core located out of a slide scar (Figure 4). The
176 core barrel bent after ca. 3 m of penetration in indurated sediment. The core is composed of

177 finely laminated silty clay in the upper 2 meters, and then a lithologic change occurs. At 2-
178 2.09 m the amount of carbonate content (bioclasts) is higher and could justify a drop in unit
179 weight value, then from 2.4 m to the base of the core several layers of fine to medium sand
180 (up to few cm thick) appear (Figure 8). Figure 8-c shows a detail of cross-laminated, mica-
181 rich, sharp-based sand layers with normal grading, that contrast with the alternating mud with
182 very thin silt laminae of the upper part of the core (Figure 8-a and -b). Moderate bioturbation
183 is present in the upper 10 cm and much more developed in the lower unit, where it disrupts
184 the geometry of some of the sand layers.

185 Core MD05-2981 recovered 10.66 m of sediment on the basin floor at about 14 km from
186 the foot of the slope affected by the landslides and seaward of the blocks/bulges (Figure 4).
187 The whole core is composed of alternating mud with sets of silt to very fine sand laminae.
188 The thickest sand layers is 20 cm, but the most common deposits are 2 to 5 mm thick silt to
189 very fine sand layers occurring in sets of 5 to 15 cm separated by 20 to 40 cm thick intervals
190 of mud (Figure 6-c). The layers are downwarped all along the core, with deformation up to 5
191 cm from the center of the core to the sides, due to piston suction. However, the overall
192 stratigraphic succession of this core is preserved and represents alternating thin-bedded
193 turbidites with possible hemipelagic sediment corresponding to plane parallel layering on 3.5
194 kHz profiles.

195 Figure 9-a shows the unit weight profile obtained from the attenuation of gamma rays through
196 core MD05-2975, (core location in Figure 2). A linear increase of the unit weight with depth
197 until 1.8 mbsf is followed by constant values down to 4 mbsf and then a decrease down to the
198 base of the core. This shape of the unit weight profile is similar for other physical
199 measurements carried out on core MD05-2975 as the P-wave velocity (Figure 9-b) and the
200 undrained shear strength (Figure 9-d). As expected, the water content (Figure 9-c) and the
201 liquidity index (Figure 9-d) display an opposite profile.

202 The unit weight and the P wave profiles of the core MD05-2972 presented in Figure 10-a and
203 Figure 10-b shows a continuous increase with depth. The water content and the liquidity
204 index profiles show a continuous decrease with depth (Figure 10-c and Figure 10-d). The
205 undrained shear strength profile shows also a linear increase with depth (Figure 10-e) but at
206 the bottom of the core we measured undrained shear strength of about 40 kPa which
207 demonstrates the highly overconsolidated state of the sediment at around 2.8 mbsf.

208 The unit weight profile from the core MD05-2981 shows constant values of the unit weight
209 all over the 10.7 m core length. The absence of any unit weight gradient demonstrates the
210 underconsolidated state of the sediment at MD05-2981 site.

211 *Compressibility and permeability tests*

212 The compressibility tests were carried out using the oedometer with incremental loading. Six
213 oedometer tests were carried out on samples from cores MD05-2972 and MD05-2975. The
214 main aim of these oedometer tests is to evaluate the consolidation state of the sediment.
215 Results of the consolidation tests in terms of compressibility for core MD05-2975 are
216 presented in Figure 11-a. Sediment sample from the level 4 mbsf is characterized by high
217 initial void ratio and a high compressibility. Permeability coefficients of the sediment from
218 cores MD05-2972 and MD05-2975 were also determined at different consolidation state and
219 different porosity. Figure 11-b shows the variation of the permeability coefficients as a
220 function of the void ratio indicating a quasi-constant slope variation for the 4 samples from
221 MD05-2975.

222 Figure 12 shows the Over-Consolidation Ratio (OCR) derived from the oedometer tests
223 indicating that the sediment from core MD05-2972 and the upper sediment from core MD05-
224 2975 are in an Over-Consolidation state. Sediment from core MD05-2975 at around 4 mbsf
225 indicates a low OCR which is probably the expression of the remolded state of the sediment at
226 this level. The origin of the high Over-Consolidation could be the stress tensor generated by

227 the upper movement of the ridge and the erosion. If it is the case, it is obvious that the stress
228 tensor like the ridge morphology is irregular and the stress is higher at the site MD05-2972
229 (maximum OCR= 6.8) than at the site of MD05-2975 (2.9).

230 **Piezometer**

231 Figure 13 shows the dissipation of the initial impulsion (temperature and pore pressure)
232 generated by the penetration of the piezometer MD05-PZ1. The MD05-PZ1 piezometer was
233 3.51 m long and it was equipped with three sensors (at -0.51 m, -2.01 m and -3.51 m from
234 the top of the lance, which corresponds to the seafloor once the piezometer stops penetrating).
235 The dissipation curves of the pore pressure presented in Figure 13 depend mainly on the
236 hydraulic permeability of the sediment. The temperature and pore pressure at equilibrium are
237 estimated from values of Figure 13 by drawing the excess pore pressure and the temperature
238 versus the reciprocal of time and extrapolating these values to $1/\text{time}=0$ (Figure 14).

239 Figure 15-a shows the excess pore pressure versus depth at site MD05-PZ1. The comparison
240 between the hydraulic gradient obtained from MD05-PZ1 and the vertical effective stress
241 obtained from the unit weight of the core MD05-2975 shows that the pore pressure at 3.51
242 mbsf (around 13.5 kPa) corresponds to about 65% of the vertical lithostatic stress. Figure 15-b
243 shows the temperature versus depth at the site MD05-PZ1. The thermal gradient derived from
244 the temperature measurements is around $182^{\circ} \text{Km}^{-1}$ and is more than three times higher than
245 the background thermal gradients measured from the study area [*Sibuet et al., 2005*].

246 **DISCUSSION**

247 **Seafloor morphologic features**

248 From the morphology presented in Figure 2 and Figure 4 it is clear that several phases of
249 failure have contributed to the present morphology of the studied ridge. At least three distinct
250 slides, that may or may not have occurred at the same time and under the same triggering

251 mechanism, are shown in Figure 4. Several other landslides inside and outside the three main
252 landslides are also indicated in Figure 4 (points A2, A3, B1, C1, D1, D2, E2, E3).

253 From Figure 6, it seems that several small blocks possibly associated with a major landslide
254 event were present before the development of a more recent sediment accumulation (Figure 6-
255 b). According to *Henstock et al. [2006]*, those positive relieves are originated from the ridge
256 flank and have probably traveled up to 15 km from the headwall scarp. Figure 2-a shows a
257 major NS trend identified as the surface expression of a N-S oriented fracture zone already
258 identified by *Sibuet et al. [2006, submitted]*. N-S fracture zones were mapped by *Deplus et al.*
259 *[1998]* in the Wharton Basin as elongated topographic features (100s of km long) as observed
260 in Figure 2-a. Even if the whole sediment thickness is higher than 2 km above the basement
261 (as mapped by *Deplus et al., [1998]*), the alternating hemipelagic and turbiditic style of
262 deposition in the deep basin favoured the persistence through time of these basement ridges.

263 In addition, if we compare the size of the aligned three large morphologic features with the
264 topographic profiles across the scar, it seems that they are too large to be considered as slided
265 blocks coming from this scar. Therefore and contrary to the *Henstock et al. [2006]*
266 conclusion, we interpret the three larger topographic features aligned along this fracture zone
267 (Figure 2-b) as possible remnants of the morphological expression of underlying basement
268 ridge. In this case, only the minor blocks located east of the fracture zone would be
269 considered as slided blocks.

270 We show on Figure 2-a the location and magnitude of aftershocks recorded in this area during
271 the « Sumatra Aftershocks » cruise, from July 22, 2005 to August 3, 2005 [*Sibuet et al., 2006*
272 *submitted*]. As the location of the aftershocks was calculated with a 1-D velocity model, the
273 spatial error might be in the order of 20 km. Some 186 aftershocks appear in a cluster located
274 just north of the *Henstock et al. [2006]* slope failure (Figure 2-a). Within this error range most
275 of the remaining aftershocks might be related to the identified N-S fracture zone. The

276 aftershocks are located either within the sedimentary cover or more probably within the
277 underlying oceanic crust. As this portion of oceanic plate is located above the diffuse
278 India/Australia plate boundary identified between the Investigator failure zone and the Ninety
279 East Ridge (90°E) where the N-S velocity vector decreases westward from 1 cm/yr to zero,
280 earthquakes within this stripe display N-S left-lateral strike-slip mechanisms [*Delescluse and*
281 *Chamot-Rooke, 2007*]. We conclude that this fracture zone was reactivated at least during the
282 recording period, releasing the accumulated stress within the transition zone as expected
283 during an inter-seismic period [*Engdahl et al., 2007* and *Sibuet et al., 2006 submitted*] or
284 more probably as a 2004 Great Sumatra Earthquake post-seismic released strain.

285 **Excess pore pressure: source and regime**

286 The excess pore pressure measured at site MD05-2975 could be the result of several events
287 and distinct triggering mechanisms. In the following we will focus on four questions: 1) Is the
288 excess pore pressure profile in a steady state or a transient regime? 2) Is the excess pore
289 pressure related to the December, 26 Great Sumatra Earthquake? 3) What is the source of the
290 excess pore pressure? and 4) Is there any link between the measured excess pore pressure and
291 one of the observed landslide?

292 *Excess pore pressure: steady state versus transient regime*

293 For an hydraulic steady state regime and by neglecting the storage effects, the Darcy equation
294 and the flow continuity lead to:

$$295 \quad k \frac{\partial h}{\partial z} = \text{constant} \quad [1]$$

296 Where k is the sediment permeability coefficient and h is the hydraulic head. Properties and
297 parameters used in this study are listed in Table 1.

298 By applying equation [1] for the *in situ* pore pressure measurements presented in Figure 15-a,

299 one can expect for a steady state regime a rate of 119 $(= \frac{\Delta h}{\Delta z} \Big|_{\text{below } 3.5\text{m}} = \frac{13.2-1.3}{1.5})$ between

$$\frac{\Delta h}{\Delta z} \Big|_{\text{above } 3.5\text{m}} = \frac{1.3-1.2}{1.5}$$

300 the permeability coefficient above and below 3.5 m. On the other hand, permeability
301 measurements carried out on samples from MD05-2975 do not show any important
302 permeability discontinuity all over the core (see Figure 11-b). This inconsistency between
303 flow continuity constrained by the hydraulic steady state regime and the measured
304 permeability coefficients clearly shows that the hydraulic regime in the upper sediment is in
305 transient regime and the hydraulic equilibrium is not yet reached.

306 For the transient regime, the one-dimensional transient fluid flow is described by:

307
$$\frac{\partial U(z,t)}{\partial t} = \frac{\partial}{\partial z} D_h(z) \frac{\partial U(z,t)}{\partial z} \quad [2]$$

308 where $D_h(z)$ represents the hydraulic diffusivity of the sediment and is directly related to the
309 permeability coefficient. $U(z,t)$ is the excess pore pressure which varies with the time t and
310 the depth in the vertical direction z .

311 As a hypothesis, we consider an initial excess pore pressure profile corresponding to 90 % of
312 the lithostatic stress in the area where we have identified the remolded sediments (Figure 16-
313 a). We also suppose that this initial state of the pore pressure build-up corresponds to the 26th
314 of December 2004 earthquake. The void ratio and the permeability design profiles (Figure 16-
315 b and -c) were computed from the unit weight profile of core MD05-2975 (Figure 9-a) and the
316 permeability coefficients values presented in Figure 11-b.

317 Using equation [2], with the initial pore pressure presented in Figure 16-a and the two design
318 profiles of the void ratio and the permeability coefficients presented in Figure 16-b and Figure
319 16-c, it is possible to determine the evolution of the pore pressure profile as a function of time

320 (Figure 16-a). The pore pressure profile computed 218 days after the Great Sumatra
321 Earthquake corresponds to the period of the *in situ* pore pressure monitoring (Figure 16-a).
322 Figure 16-a shows a very good agreement between the predicted excess pore pressure and the
323 *in situ* pore pressure measured during the “Sumatra Aftershocks” cruise. Several calculations
324 were carried out in order to identify the most suitable initial excess pore pressure. We find
325 that 90 % of the vertical lithostatic stress is the most suitable value to explain our pore
326 pressure measurements. This good agreement between calculated and measured excess pore
327 pressure demonstrates that the high excess pore pressure was generated at the time of the
328 December, 26 Great Sumatra Earthquake.

329 The shape of the thermal gradient (linear) measured at MD05-PZ1 differs from the one of the
330 pore pressure. The origin of the high thermal gradient and of the high hydraulic gradient at the
331 site MD05-PZ1 is therefore not the same. Indeed, the linear shape of the thermal gradient
332 suggests that the temperature field in this area presents a permanent regime over the first 3.5
333 m while the hydraulic gradient corresponds to a transient regime. The high linear increase of
334 the temperature with depth must be related to continuous inter-seismic movements along a
335 slip plane and not to a unique catastrophic movement as in the case of an earthquake.

336 *Pore pressure source: earthquake shaking or slab subduction?*

337 Sediment, when exposed to strong earthquake ground shaking, undergoes compaction, and the
338 grains squeeze together, taking up less space. Since the duration of the cyclic loading from an
339 earthquake is too short to ensure the drainage of interstitial water, a decrease in the effective
340 confining stress and a consequent increase of equal magnitude in the pore water pressure will
341 occur. When the sand is loose enough and the magnitude of the cyclic shear stress is high
342 enough, the vertical effective stress drops to zero. For sands and silty sands, this phenomenon
343 is known as sediment liquefaction and is generally associated with slope instabilities,
344 sediment failures, ground settlement, and occasionally sand boils. For soft clays, cyclic

345 loading generated by an earthquake may induce the degradation of sediment stiffness and
346 shear strength [*Idriss et al.; 1976 and 1978*], but also an increase in pore pressure [*Biscontin*
347 *and Pestana, 2006*].

348 Alternatively, slab subduction produces excess pore pressures independently of earthquakes
349 process: high porosity sediment is dragged down under the accretionary prism leading water
350 to squeeze out from sediment and pressurizing the entire prism [*Von Huene and Lee, 1982;*
351 *Saffer et al., 2000*]. Therefore, the main question remains whether the origin of the monitored
352 excess pore pressure is related to slab subduction or to the earthquake shaking?

353 One of the main divergences between these two processes (earthquake versus slab
354 subduction) is the position of the pore pressure source. While the pore pressure source is deep
355 and generated at or below the décollement zone for subduction, it is contained in the upper
356 soft sediment for earthquake cyclic loading [*Biscontin et al., 2006*]. Modeling results
357 presented in Figure 16-a show that the measured pore pressure could be a direct consequence
358 of the December, 26 Great Sumatra Earthquake. In the following, a deep source pore pressure
359 will be considered to evaluate any possible link between the measured pore pressure and the
360 deep slab subduction movement.

361 Sediment porosities and permeabilities from the margin wedge above the décollement surface
362 are expected to decrease with depth below the seafloor. Therefore, we can anticipate an

363 increase of the pore pressure gradient ($\frac{\partial U(z,t)}{\partial z}$) with depth in order to insure the flow

364 continuity. Our working hypothesis is to consider over the margin wedge a lithology similar
365 to core MD05-2975. From the porosity, the permeability and the bulk unit weight of the
366 sediment, it is possible to quantify by a back analysis the evolution of the excess pore
367 pressure and the stress state over the geological formation. For that, the principle of the
368 effective stress that defines the vertical effective stress in porous media (σ'_v) as the difference
369 between the vertical total stress (σ_v) and pore fluid pressure (u) is used:

370
$$\sigma'_v = \sigma_v - u \quad [3]$$

371 In equation 3, the pore fluid pressure u is the sum of the hydrostatic pressure ($\rho_w g z$) and the
372 excess pore pressure (U) with ρ_w is the water unit weight and g the gravitational constant

373
$$u = U + \rho_w g z \quad [4]$$

374 The link between the void ratio e and the vertical effective stress is considered through the
375 following equation:

376
$$e = e_0 - \lambda \cdot \ln\left(\frac{\sigma'_v}{\sigma'_0}\right) \quad [5]$$

377 where e_0 is a reference void ratio at a reference vertical effective stress σ'_0 , and λ is the
378 compression index.

379 The vertical effective stress, the porosity, the permeability coefficient, the hydraulic
380 diffusivity and the thermal diffusivity are calculated using the principle of the effective stress
381 (eq. 3) and the compressibility curves (eq. 5) defining the link between the void ratio e and
382 the vertical effective stress. The compressibility index λ is determined from Figure 11-a.

383 Three source depths of the pore pressure are considered: at 100 meters below seafloor (mbsf),
384 50 mbsf and 25 mbsf. For each pore pressure sources, the amount of the excess pore pressure
385 is supposed to be equal to 25 %, 50 %, 85 % and 95 % of the lithostatic stress. The calculation
386 results of the pore pressure profiles are presented in Figure 17-a (source at 100 mbsf), Figure
387 17-b (source at 50 mbsf) and Figure 17-c (source at 25 mbsf). For the twelve calculations, the
388 calculated excess pore pressure diverges from the observed one showing that either the source
389 (location and amplitude) of the excess pore pressure or the used permeability profile are not
390 compatible with the measured excess pore pressure.

391 Other hypothesis is to consider that the permeability coefficient could be strongly modified by
392 the high excess pore pressure. Indeed, hydro-fracturing could be generated when the
393 difference between the fluid pressure and least principal (confining) stress becomes close to

394 zero. Hydro-fracturing generates Mode I fractures (displacement perpendicular to fracture)
 395 and can induce a drastic increase of the permeability of the medium. Figure 18-a shows the
 396 pore pressure profile calculated for a permeability increase ($5 \cdot 10^{-5}$ m/s) generating hydro-
 397 fracturing below 5 m. A relatively good agreement can be observed between the measured
 398 pore pressure and the calculated one (Figure 18-a). On the other hand, the hydro-fracturing
 399 which can be derived from the permeability coefficient and the hydraulic head will generate
 400 high Darcy velocities $v(z)$:

$$401 \quad v(z) = k(z) \frac{\partial h}{\partial z} \quad [6]$$

402 Temperature field can be also used to verify the hypothesis of a deep pore pressure source.
 403 Indeed, water advection from hot deep décollement level can be the cause of an increase of
 404 the thermal gradient. For steady-state thermal regime, the temperature can be evaluated by the
 405 following equation:

$$406 \quad \frac{\partial}{\partial z} \left(D_T(z) \frac{\partial T}{\partial z} \right) = v(z) \frac{\partial T}{\partial z} \quad [7]$$

407 with $D_T(z)$ corresponding to the thermal diffusivity and $v(z)$ to the vertical water velocity.

408 Because the hydro-fracturing and the high Darcy velocities, the temperature profile calculated
 409 using equation 7 and presented in Figure 18-b highly overestimates the *in situ* measured
 410 temperature. Thus, the high permeability generated by hydro-fracturing and the deep pore
 411 pressure source at the subduction level can be also ruled out.

412 *Excess pore pressure and sediment deformation*

413 The pore pressure measurements and the calculation results show that the most likely origin
 414 of the excess pore pressure seems to be a local deformation of the upper sediment layers
 415 generated in the same time-period of the December, 26 Great Sumatra Earthquake. The build-
 416 up pore pressure during the earthquake was certainly higher than the value measured in July
 417 2005. From the calculation it was evaluated to be around 90 % of the lithostatic stress. The

418 high residual excess pore pressure measured in July 2005 is a clear indication of a local
419 sediment deformation without any slope failure generation at the MD05-PZ1 site. For any
420 submarine slope with a normally consolidated soil and a slope angle larger than 10 degrees as
421 it is shown in Figure 5-c, an important build up pore pressure as the one measured at MD05-
422 PZ1 will certainly cause a slope to fail. For the MD05-PZ1 area, the highly over-consolidated
423 upper sediment (Figure 12) has probably prevented the slope failure to occur.

424 OCR values obtained from MD05-2975 and MD05-2972 cores have shown two different state
425 of consolidation at the two different sites. This different consolidation state is obviously
426 related to the irregular ridge morphology and erosion: core MD05-2972 recovered ancient
427 sediment coming from the erosion and denudation of the inner part of an anticline, MD05-
428 2975 sampled likely younger sediment. Sediments previously positioned within the present
429 scars (slide scar 2 and 3 - Figure 2) were probably less consolidated than the sediment from
430 MD05-2975 and MD05-2972 cores and have probably reached failure and flowed along the
431 slope under the excess pore pressure generated by the December, 26 Great Sumatra
432 Earthquake. The sediment flow indicated in Figure 6-b could be the result of such slope
433 failure.

434 **CONCLUSION**

435 The bathymetric data acquired during the “Sumatra Aftershocks” cruise show the existence of
436 several scars and deposits with a ‘fresh’ aspect caused by likely recent slope failures in the
437 study area from the base of continental rise up to the accretionary prism and the continental
438 slope flanking the Aceh forearc basin. The fact that no evidence of a very large and recent
439 submarine landslide was found could be explained by the high frequency of high-magnitude
440 seismic events occurring in the study area. This recurrence of events might favor the presence
441 of numerous small-scale rather than few large landslides. The landslide identified by
442 [Henstock et al. \[2006\]](#) seems to be the result of several phases of failure. Several blocks,

443 probably related to the main landslide described by *Henstock et al. [2006]*, were identified in
444 the deep depositional area. From the 3.5 kHz profile data it seems clear that these blocks are
445 the expression of several ancient events rather than one recent landslide. On the other hand,
446 three large topographic features aligned along an N-S fracture zone may be interpreted as a
447 remnant morphological expression of a buried basement ridge.

448 Core MD05-2975 recovered from the slope located north of the HMS Scott landslide
449 [*Henstock et al., 2006*] indicates the existence of remolded sediment. The *in situ* pore pressure
450 monitoring using a piezometer at the same site demonstrates that an excess pore pressure was
451 generated by a recent event. The calculation results have shown that the excess pore pressure
452 is in a transient regime. Moreover, the pore pressure measurements and the calculation results
453 show that the most likely origin of the excess pore pressure seems to be a local deformation of
454 the upper sediment layers generated in the same time-period than the December, 26 Great
455 Sumatra Earthquake.

456 Two different consolidation states were identified from core MD05-2975 and MD05-2972
457 and are probably related to the differential ridge erosion and morphology: core MD05-2972
458 recovered ancient sediment coming from the erosion and denudation of the inner part of an
459 anticline, MD05-2975 sampled likely younger sediment. Due to the differential upward
460 movement of the ridge, it is expected less over-consolidated sediment at the site where the
461 three main landslides were identified. In the area of the three identified landslides, the high
462 excess pore pressure measured at MD05-PZ1, could be enough to generate sediment failure
463 and accumulation at the toe of the slope, as observed on 3.5 kHz profiles.

464 Finally, the high thermal gradient and the high hydraulic gradient at Site MD05-PZ1 certainly
465 represent the expression of two distinct phenomena. Indeed, while the thermal gradient
466 presents a permanent regime over the first 3.5 m (linear temperature profile), the hydraulic
467 gradient corresponds to a transient regime. The high linear increase of the temperature with

468 depth must be related to continuous inter-seismic movements along a slip plane and not to a
469 unique catastrophic movement as in the case of an earthquake.

470 **ACKNOWLEDGEMENTS**

471 The “Sumatra Aftershocks” cruise was organized in collaboration between the Institut
472 Français de Recherche pour l’Exploitation de la Mer (Ifremer), the Institut Polaire
473 Français - Paul Emile Victor (IPEV) and the Agency for the Assessment and
474 Application of Technology, Indonesia (BPPT). We thank captain François Duchene and
475 the crew of the R/V Marion Dufresne for their dedicated work during the MD149
476 «Sumatra Aftershocks» cruise, as well as the technical staff of the Institute Paul-Emile
477 Victor (IPEV) led by B. Ollivier for their constant and precious help. Financial supports
478 were provided by the Agence Nationale de la Recherche (ANR), the Délégation Inter-
479 ministérielle pour le Tsunami (DIPT), Ifremer and IPEV.

480 # ‘Sumatra Aftershocks’ team: J.-C. Sibuet, S. Singh, R. Apprioual, N.C. Aryanto, J. Begot,
481 A. Cattaneo, A.P.S. Chauchan, R. Creach, J. Crozon, A. Domzig, N. Falleau, D. Graindorge,
482 F. Harmegnies, Y. Haryadi, F. Klingelhoffler, S.K. Kolluru, J.-Y. Landuré, C. Le Lann, J.
483 Malod, A. Normand, G. Oggian, C. Rangin, D. Restunin Galih, J.-L. Schneider, N. Sultan, M.
484 Taufik, M. UMBER and H. Yamaguchi.

485 **REFERENCES**

- 486 Bilham, R., R. Engdahl, N. Feldl, and S.P. Satyabala (2005), Partial and Complete Rupture of the
487 Indo-Andaman Plate Boundary 1847-2004, *Seismological Research Letters*, 76, 299-311.
488
- 489 Biscontin, G., and J.M. Pestana (2006), Factors affecting seismic response of submarine slopes, *Natural*
490 *Hazards and Earth System Sciences*, 6, 97-107.
491
- 492 Davis, E.E., G.C. Horel, and R.D. MacDonald (1991), Pore pressures and permeabilities measured in
493 marine sediments with a tethered probe, *Journal of Geophysical Research*, 96, 5975-5984.
494
- 495 de Groot-Hedlin, C.D (2005), Estimation of the rupture length and velocity of the Great Sumatra
496 earthquake of Dec 26, 2004 using hydroacoustic signals, *Geophysical Research Letters*, 32,
497 doi:10.1029/2005GL022695.
498
- 499 Delescluse, M., and N. Chamot-Rooke (2007). Instantaneous deformation and kinematics of the India-
500 Australia plate, *Geophys. J. Int.*, 168, 818-842.
501
- 502 Deplus, C., M. Diamant, H. Hébert, B. Bertrand, S. Dominguez, J. Dubois, J. Malod, P. Patriat, B.
503 Pontoise, and J.-J. Sibilla (1998). Direct evidence for active deformation in the eastern Indian Ocean
504 plate, *Geology*, 26, 131-134.
505
- 506 Engdahl, E. R., A. Villasenor, H. R. DeShon, and C. H. Thurber (2007). Teleseismic Relocation and
507 Assessment of Seismicity (1918-2005) in the Region of the 2004 *Mw* 9.0 Sumatra-Andaman and
508 2005 *Mw* 8.6 Nias Island Great Earthquakes, *Bull. Seism. Soc. America*, 97, 43-61.
509
- 510 Fang, W.W., M.G. Langseth, and P.J. Schultheiss (1993), Analysis and application of in situ pore
511 pressure measurements in marine sediments, *Journal of Geophysical Research*, 98, 7921-7938.
512
- 513 Fine, I.V., A.B. Rabinovich, B.D. Bornhold, R.E. Thomson, and E.A. Kulikov (2005), The Grand
514 Banks landslide-generated tsunami of November 18, 1929: preliminary analysis and numerical
515 modeling, *Marine Geology*, 215, 45-57.
516
- 517 Hébert, H., F. Schindelé, Y. Altinok, B. Alpar, C. Gazioglu (2005), Tsunami hazard in the Marmara
518 Sea (Turkey): a numerical approach to discuss active faulting and impact on the Istanbul coastal areas,
519 *Marine Geology*, 215, 23-43.
520
- 521 Henstock, J.H., L.C. McNeil, and D.R. Tappin (2006), Seafloor morphology of the Sumatran
522 subduction zone: surface rupture during megathrust earthquakes?, *Geology*, 34, 485-488.
523
- 524 Idriss, I.M., R. Dobry, E.H. Doyle, and R.D. Singh (1976), Behavior of soft clays during earthquake
525 loading conditions, *In Proceedings of the Offshore Technology Conference*, Houston, Texas, OTC
526 2671, Vol. 3.
527
- 528 Idriss, I.M., R. Dobry, and R.D. Singh (1978), Nonlinear behavior of clay soils during cyclic loading,
529 *Journal of the Geotechnical Engineering Division, ASCE*, 104(12), 1427-1447.
530
- 531 Park, J., K. Anderson, R. Aster, R. Butler, T. Lay, and D. Simpson (2005), Global Seismographic
532 Network records the Great Sumatra-Andaman Earthquake, *Eos*, 86, 57-64.
533
- 534 Pelinovsky, E., and S. Tinti (2005), Tsunamis in the Pacific, in the Atlantic and in Europe: relevant
535 cases and hazard evaluation, *Marine Geology*, 215, 106 pp.
536
537

538 Puspito, N.T. (2002), Tsunami and earthquake activity in Indonesia, In A.B. Rabinovich, W. Rapaz
539 (Eds.), Proceedings of the International Workshop 'Local tsunami warning and mitigation', September
540 10-15, 2002, Moscow, 138-145, <http://seac47-2.phys.msu.ru/proc/>
541

542 Saffer, D.M., E.A. Silver, A.T. Fisher, H. Tobin, and K. Moran (2000), Inferred pore pressures at the
543 Costa Rica subduction zone: implications for dewatering processes, *Earth and Planetary Science*
544 *Letters*, 177, 193–207.
545

546 Schultheiss, P.J., and S.D. McPhail (1986), Direct indication of pore water advection from pore
547 pressure measurements, in Madeira abyssal plain sediments, *Nature*, 320, 348-350.
548

549 Sibuet, J.-C. and the 'Sumatra Aftershocks' team' (2005), « Sumatra Aftershocks » cruise report, 105
550 pp.
551

552 Sibuet, J.-C., C. Rangin, X. Le Pichon, S. Singh, A. Cattaneo, D. Graindorge, F. Klingelhoefer, J.-Y.
553 Lin, J. Malod, T. Maury, J.-L. Schneider, N. Sultan, M. Umler, H. Yamaguchi and the "Sumatra
554 aftershocks" team (2006). 26th December 2004 Great Sumatra-Andaman Earthquake: seismogenic
555 zone and active splay faults, *Earth Planet. Sci. Lett.*, submitted.
556

557 Singh, S.C. and the Sumatra-Aftershocks Team, (2005). Sumatra earthquake research indicates why
558 rupture propagates northwards, *EOS*, 86, 497-502.
559

560 Sultan, N., M. Voisset, B. Marsset, T. Marsset, E. Cauquil, and J.L. Colliat (2007), Potential role of
561 compressional structures in generating submarine slope failures in the Niger delta, *Marine Geology*,
562 doi: 10.1016/j.margeo.2006.11.002.
563

564 Stein, S., and E.A. Okal (2005), Speed and size of the Sumatran earthquake, *Nature*, 434, 581-582.
565

566 Urgeles, R., M. Canals, and J. Roberts (2000), Fluid flow from pore pressure measurements off La
567 Palma, Canary Islands, *Journal of Volcanology and Geothermal Research*, 101, 253-271.
568

569 USGS (2005) Preliminary Earthquake Report. (U.S. Geological Survey, National Earthquake
570 Information Center, World Data Center for Seismology, Denver)
571 <http://earthquake.usgs.gov/recenteqsww/Quakes/usweax.htm>
572

573 Von Huene, R., and H. J. Lee (1982), The possible significance of pore fluid pressures in subduction
574 zones, in: Studies in continental Margin Geology, J. S. Watkins and C. L. Drake, eds., *AAPG Memoir*
575 34, 781-792.
576

577 **FIGURE CAPTIONS**

578

579 **Figure 1. a** Overview of the swath bathymetric data acquired during the “Sumatra Aftershocks” cruise
580 [*Sibuet et al., 2005*]. Black square locates the study area in the slope failure zone identified by *Henstock et*
581 *al. [2006]* and the location of Figure 2. **b)** Cross section along the acquired bathymetric data showing the
582 Aceh basin, the Sumatra accretionary prism and the trench. Black arrow (CS1) in Figure 1-a indicates the
583 location of the cross section.

584

585 **Figure 2.** 3D bathymetric map showing a slide scar in the deepest part of the bathymetric data presented
586 in Figure 1 (frontal area of the Sumatra accretionary prism) and location of cores MD05-2972, MD05-
587 2975 and MD05-2981 and piezometer MD05-PZ1. Bathymetric sections A-A to E-E are in Figure 5.
588 Aftershocks recorded in the area during the « Sumatra Aftershocks » cruise are added to the figure. Two
589 faults described in the text are traced on the map with a solid red line. Note that this figure does not
590 report all the other tectonic features identified in the area (see *Henstock et al [2006]* and *Sibuet et al.*
591 *[2005]*). Aftershock locations recorded during the “Sumatra Aftershocks” cruise are also reported as red
592 dots.

593

594 **Figure 3.** Excess pore pressure at equilibrium obtained at two different levels (a: 11.6 mbsf and b: 10.1
595 mbsf) from long-term (one week) monitoring and extrapolation. The maximum error between the real
596 and the extrapolated equilibrium pore pressures is around 0.5kPa which is comparable to the precision of
597 the pore pressure sensors.

598

599 **Figure 4.** Shaded bathymetry of the slope failure zone identified by *Henstock et al. [2006]* showing the
600 presence of at least three major sliding phases and associated blocks. Dashed lines show the location of 5
601 bathymetric cross sections presented in Figure 5. Continuous lines show the location of 3.5 kHz profiles
602 presented in Figure 6.

603

604 **Figure 5. a)** Three NE-SW cross sections across the northern part of the slope failure zone (A-A, B-B and
605 E-E) showing the boundary of the eroded ridge crest (arrows A1 and E1) and 5 landslide toes (arrows A2,
606 A3, B1, E2 and E3) already identified by *Henstock et al. [2006]* and corresponding to several phases of
607 failures. **b)** Two NE-SW cross sections across the slide 1, slide 2 and slide 3 indicated in figure 4 (C-C and
608 D-D) showing several scarps which correspond to several phases of failures. **d)** slope angle along the two
609 cross sections C-C and E-E showing that the slope angle between those two cross sections are comparable
610 and are lower than 17 degrees.

611

612 **Figure 6. a)** 3.5 kHz profile across the HMS slide scar area down to the block field and beyond (for
613 location see Figure 2). The location of cores MD05-2975 and MD05-2981 is projected. **b)** 3.5 kHz profile
614 across the block field associated to the different sliding phases from the flank of the frontal ridge (for
615 location see Figure 2). Soft sediments overlapping the blocks and an irregular, lens-shaped sediment
616 deposit seem to confirm the presence of several sliding phases of different ages. **c)** 3.5 kHz profile showing
617 that to the SW on the trench basin a seafloor escarpment with a NW-SE trend on map (Figure 2) ca. 20
618 km away from the base of the accretionary prism front. The location of core MD05-2981 is projected.

619

620 **Figure 7.** Sediment core MD05-2975 4 km upslope of ‘slide scar 3’ is presented with a synthetic lithologic
621 log, a unit weight curve and photo and/or X-ray Scopix images of selected intervals. Note the disrupted
622 sediment structures between 4.4 and 4.8 m (down core) that could represent a remolded sedimentary unit.

623

624 **Figure 8.** The synthetic lithologic log and selected photo and/or X-ray Scopix images of sediment core
625 MD05-2972 show a marked change in lithology occurs at 2 m (down core).

626

627 **Figure 9. Geotechnical and physical data obtained from core MD05-2975. a) Unit weight b) compressional**
628 **wave velocity c) water content d) liquidity index and e) undrained shear strength versus depth.**

629

630 **Figure 10. Geotechnical and physical data obtained from core MD05-2972. a) Unit weight b)**
631 **compressional wave velocity c) water content d) liquidity index and e) undrained shear strength versus**
632 **depth.**

633

634 **Figure 11. a) Oedometer tests carried out on 4 samples from MD05-2975 and b) permeability coefficients**
635 **determined for 4 samples from MD05-2975 and at different consolidation states corresponding to**
636 **different void ratios.**

637

638 **Figure 12. Over-Consolidation ratio OCR derived from oedometer tests carried out on cores MD05-2972**
639 **and MD05-2975 indicating that sediment in both cores is in Over-Consolidation state. The low OCR at**
640 **around 4 mbsf in core MD05-2975 indicates remolded sediment.**

641

642 **Figure 13. Initial impulsion and dissipation of a) the temperature and b) the pore water pressure at three**
643 **different levels generated by the piezometer MD05-PZ1 penetration (V1: 0.51 mbsf, V2: 2.01 mbsf and**
644 **V3: 3.51 mbsf).**

645

646 **Figure 14. Extrapolation of the equilibrium pore pressures at 3 different levels (V1 - 0.51 mbsf, V2 -**
647 **2.01 mbsf and V3 - 3.51 mbsf) from 3 hours of pore pressure monitoring (site MD05-PZ1 - Figure 2).**

648

649 **Figure 15. a) Excess pore pressure and b) temperature versus depth at site MD05-PZ1. Comparison**
650 **between the hydraulic gradient obtained from MD05-PZ1 and the lithostatic stress obtained from the unit**
651 **weight of the core MD05-2975 shows that the pore pressure at 3.51 mbsf corresponds to around 65% of**
652 **the lithostatic stress.**

653

654 **Figure 16. a) Excess pore pressure profile measured at MD05-PZ1 and calculated at different time-**
655 **periods. The initial excess pore pressure is supposed to correspond to 90% of the lithostatic pressure in**
656 **the area where we have identified the remolded sediment from core MD05-2975. Design profiles used in**
657 **the calculation for b) the void ratio and c) the permeability coefficient.**

658

659 **Figure 17. Excess pore pressure considered as a result of slab subduction and evaluated under a steady**
660 **state regime with a pore pressure source at a) 100 mbsf b) 50 mbsf and c) 25 mbsf. The lithology over the**
661 **calculation depth is considered as homogeneous.**

662

663 **Figure 18. Excess pore pressure considered as a result of slab subduction and evaluated under a steady**
664 **state regime. Hydro-fracturing is supposed to occur below 5 m inducing an increase of the permeability**
665 **coefficient to $5 \cdot 10^{-5}$ m/s. a) excess pore pressure calculated and measured, b) temperature profile**
666 **calculated and measured and c) Darcy velocity profile.**

667

Symbol	Definition and units
D_h	hydraulic diffusivity (m^2/s)
D_T	thermal diffusivity (m^2/s)
e	void ratio
g	gravitational constant (m/s^2)
h	Hydraulic head (m)
k	Permeability coefficient (m/s)
λ	compression index
OCR	Over-Consolidation ratio
ρ_w	water unit weight (kN/m^3)
σ'_0	reference vertical effective stress (kN/m^2)
σ'_v	vertical effective stress (kN/m^2)
σ_v	vertical total stress (kN/m^2)
t	Time (s)
u	pore fluid pressure (kN/m^2)
U	Excess pore pressure (kN/m^2)
v	Darcy velocity (m/s)
z	depth in the vertical direction (m)

668

669 **Table 1. Parameters and symbols used in this paper.**

670

671

672

673

Name	Type	Lat N	Lon E	Depth	Length
MD05-2972	Gravity	4.294	93.196	3568	2.94
MD05-2975	Gravity	4.254	93.210	3471	5.72
MD05-2981	Calypso	4.105	93.083	4501	10.66
MD05-PZ1	Piezometer	4.255	93.213	3484	3.5

674

675 **Table 2. Basic information on the sediment cores from the “Sumatra Aftershocks” campaign.**

676

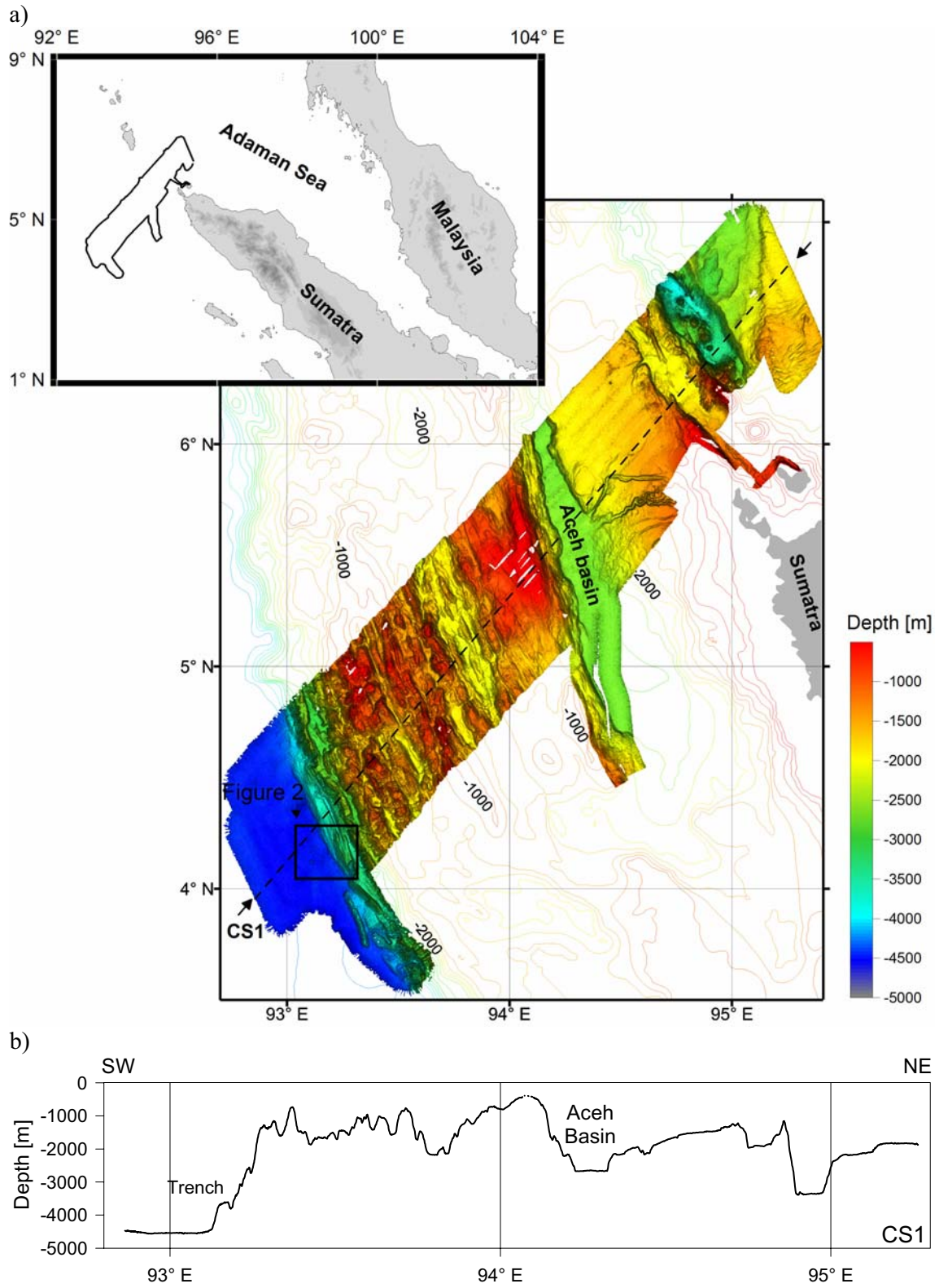


Figure 1.

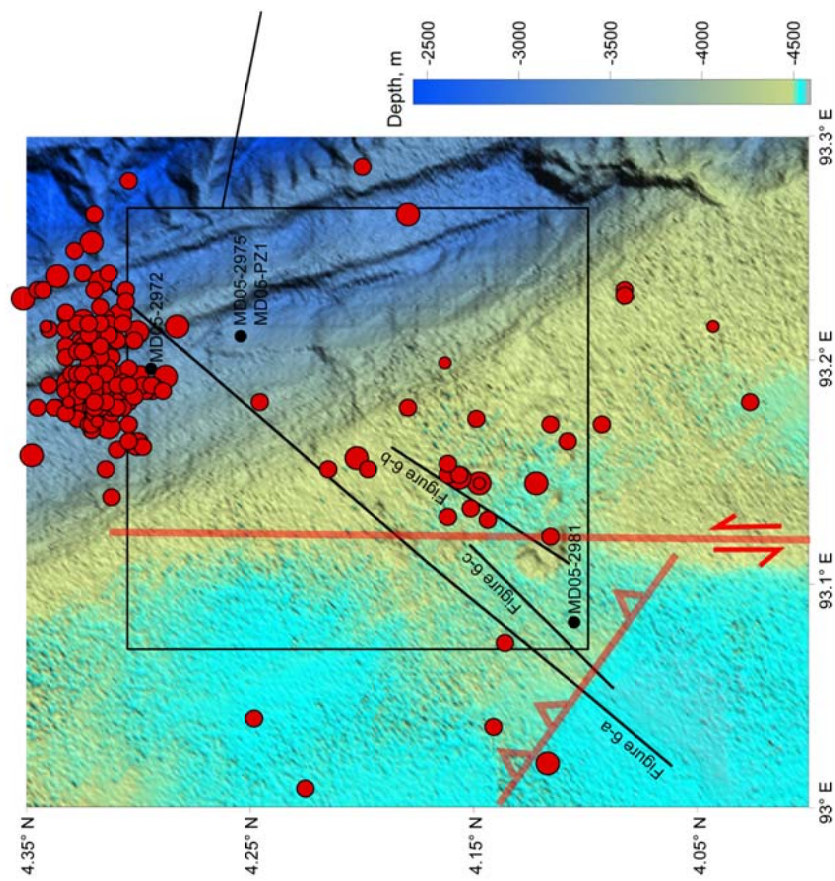
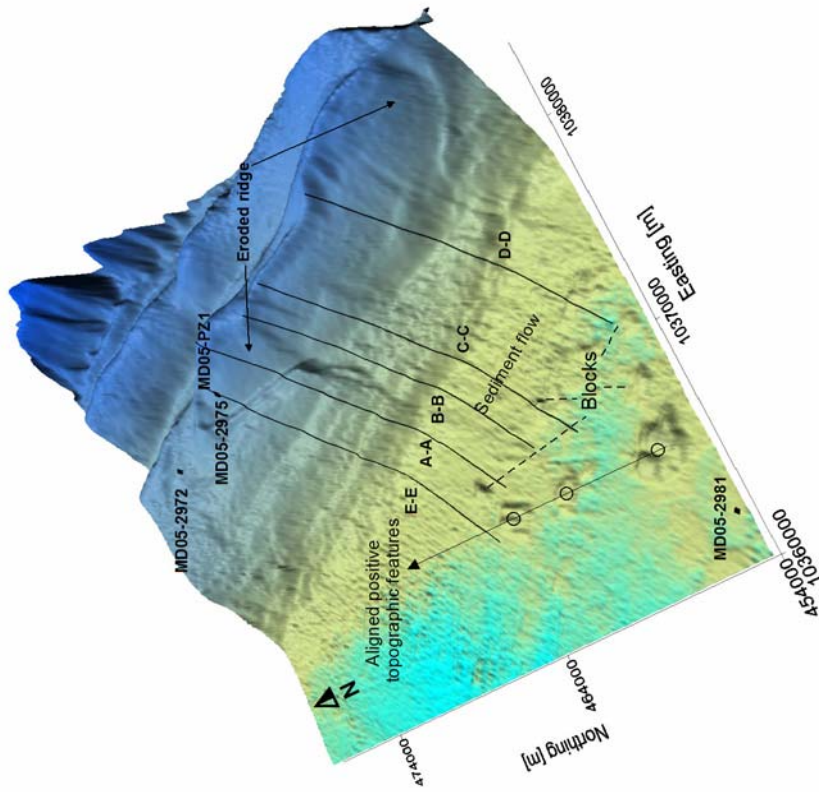


Figure 2.

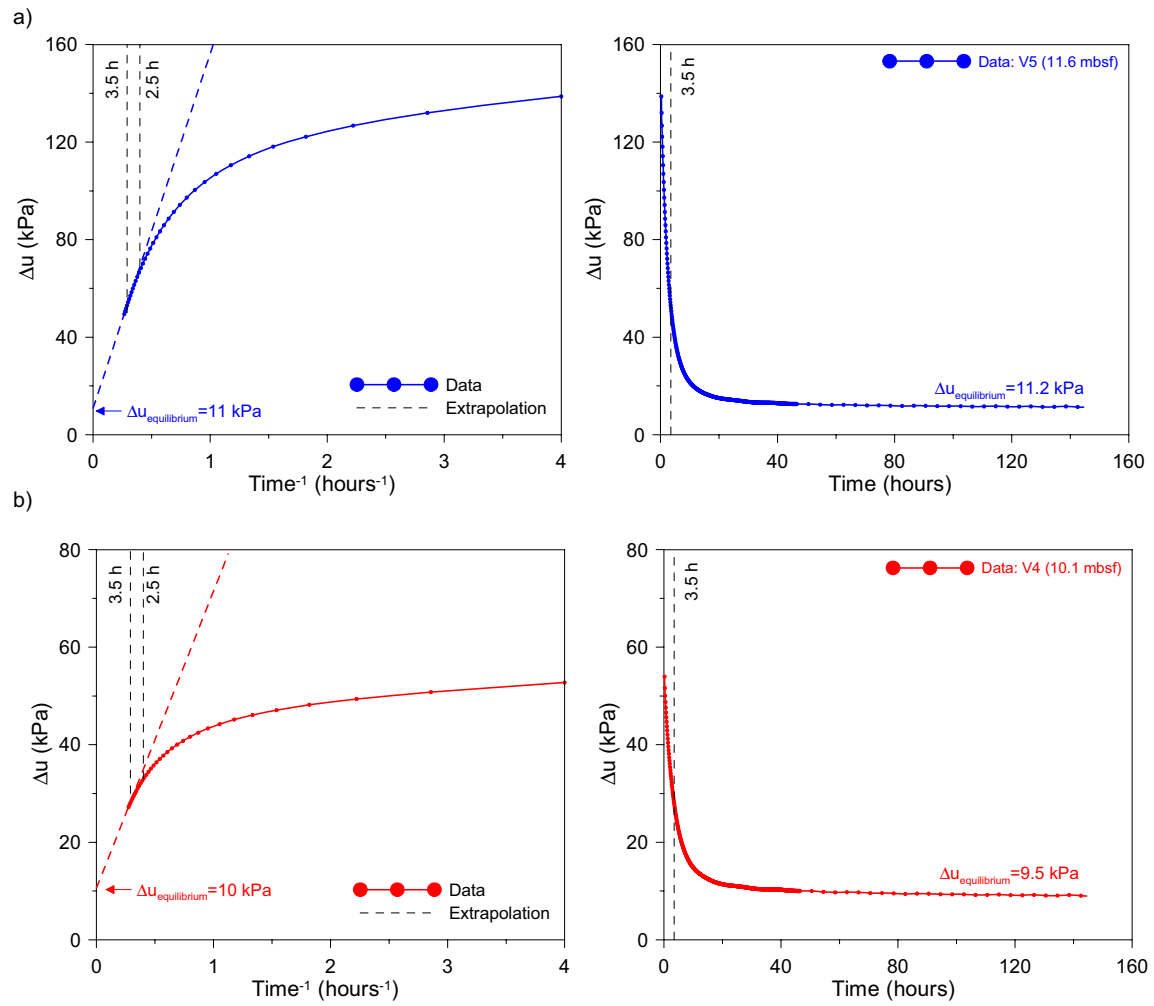


Figure 3.

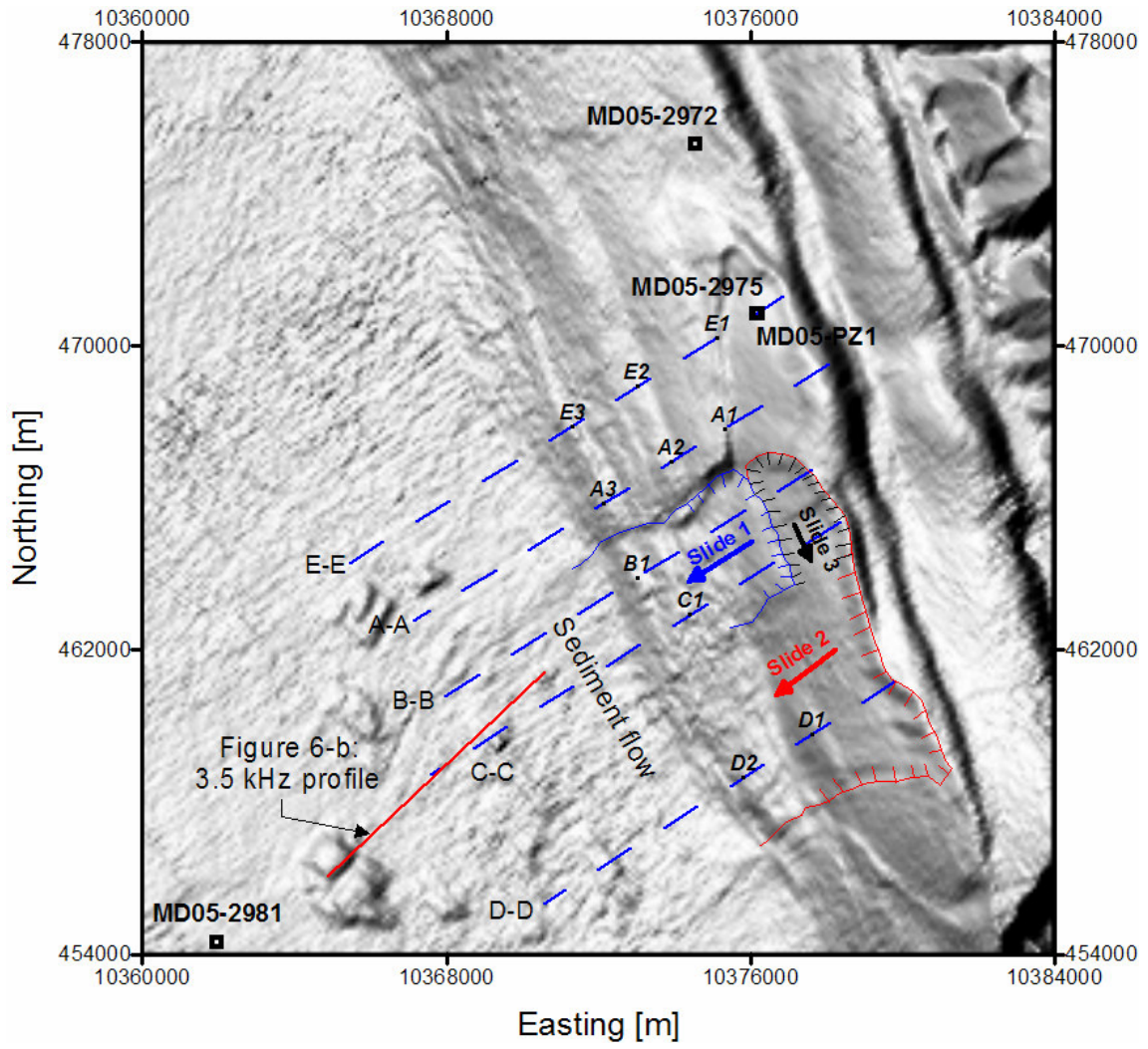


Figure 4.

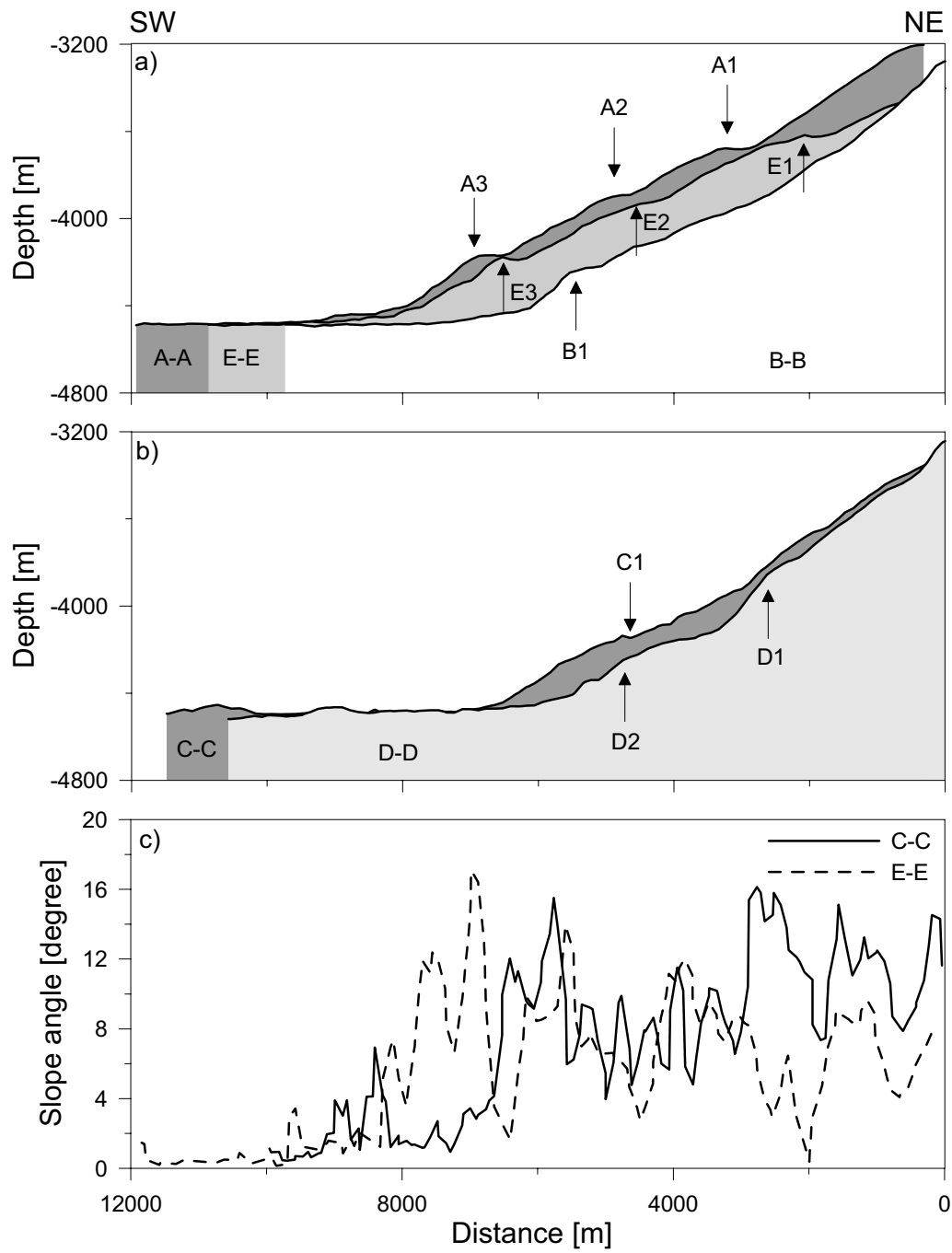
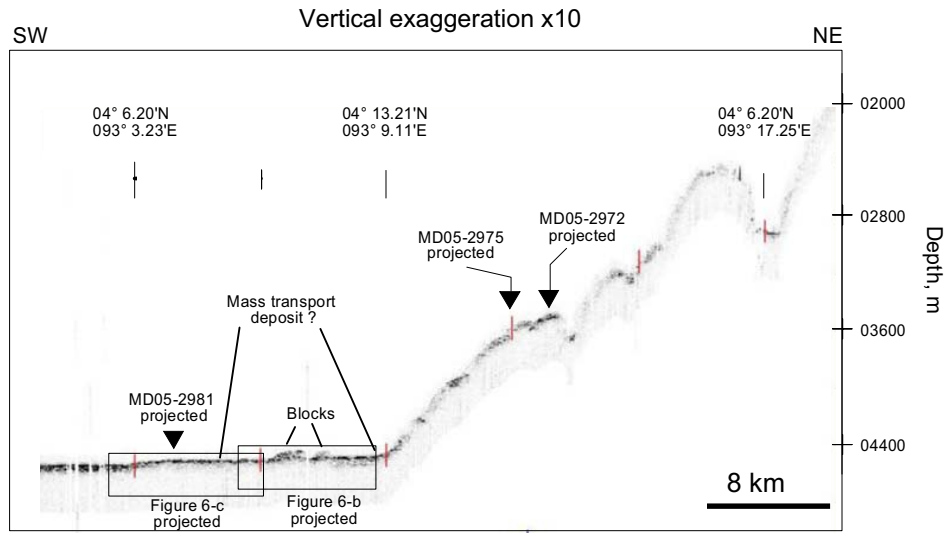
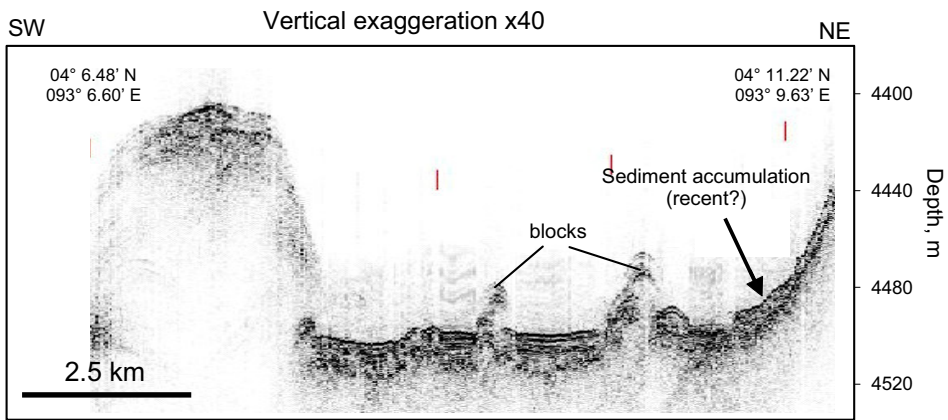


Figure 5.

a)



b)



c)

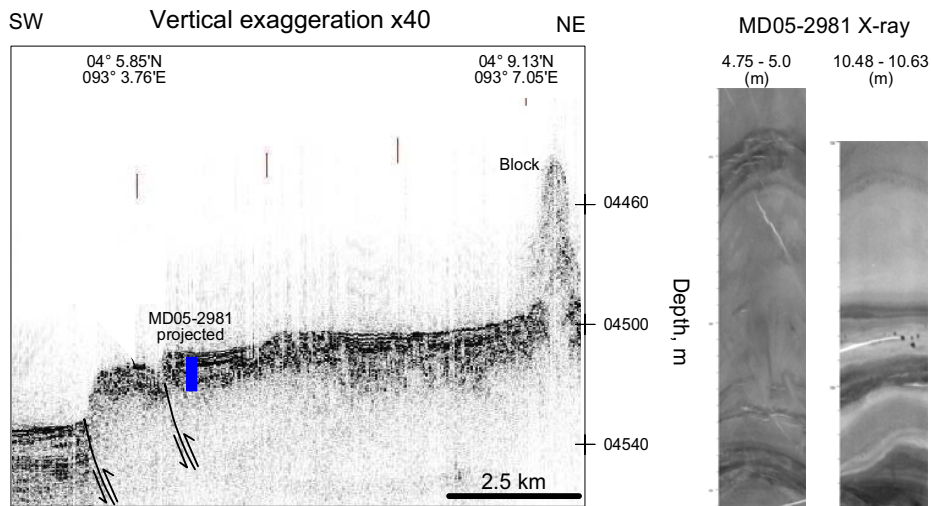


Figure 6.

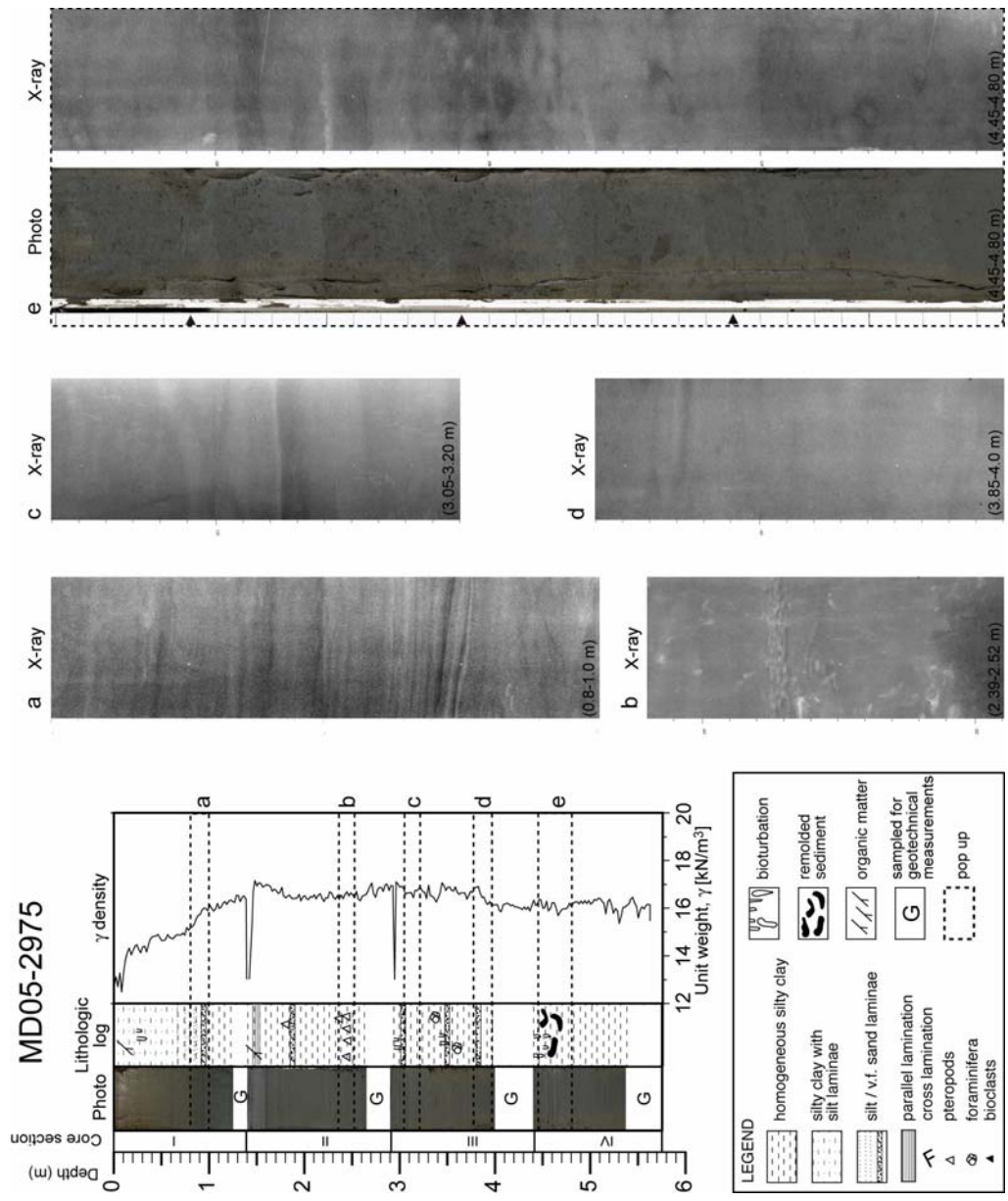


Figure 7.

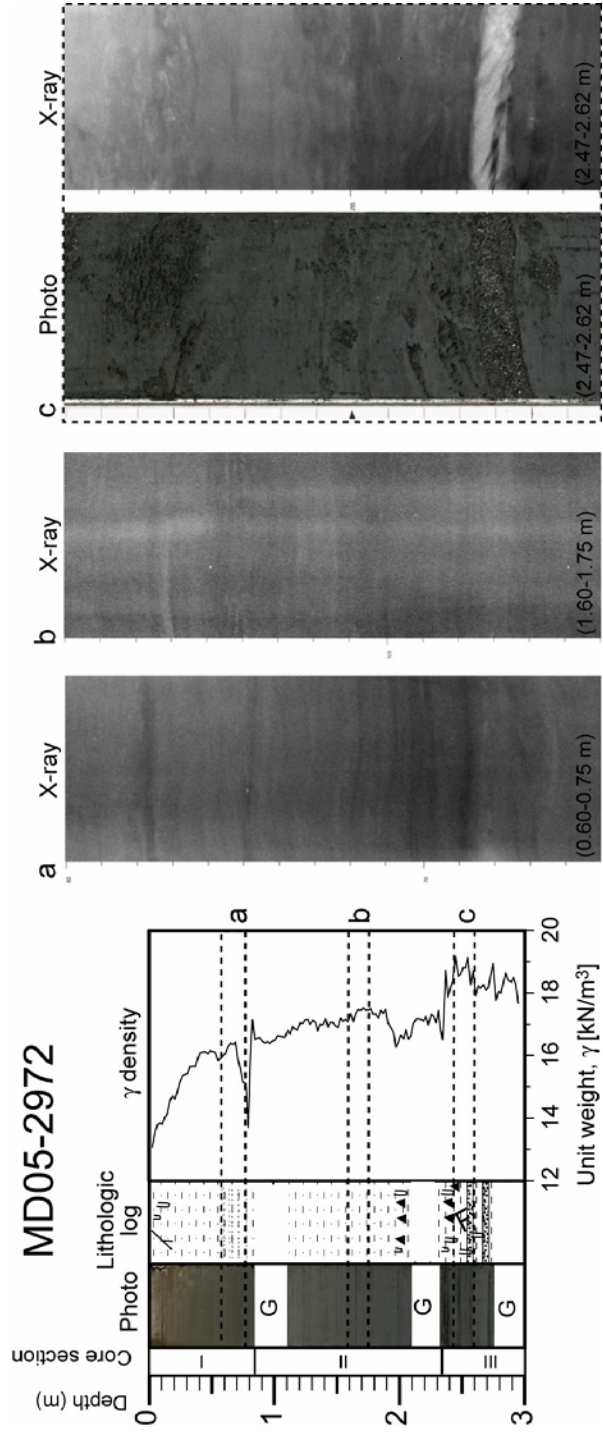


Figure 8.

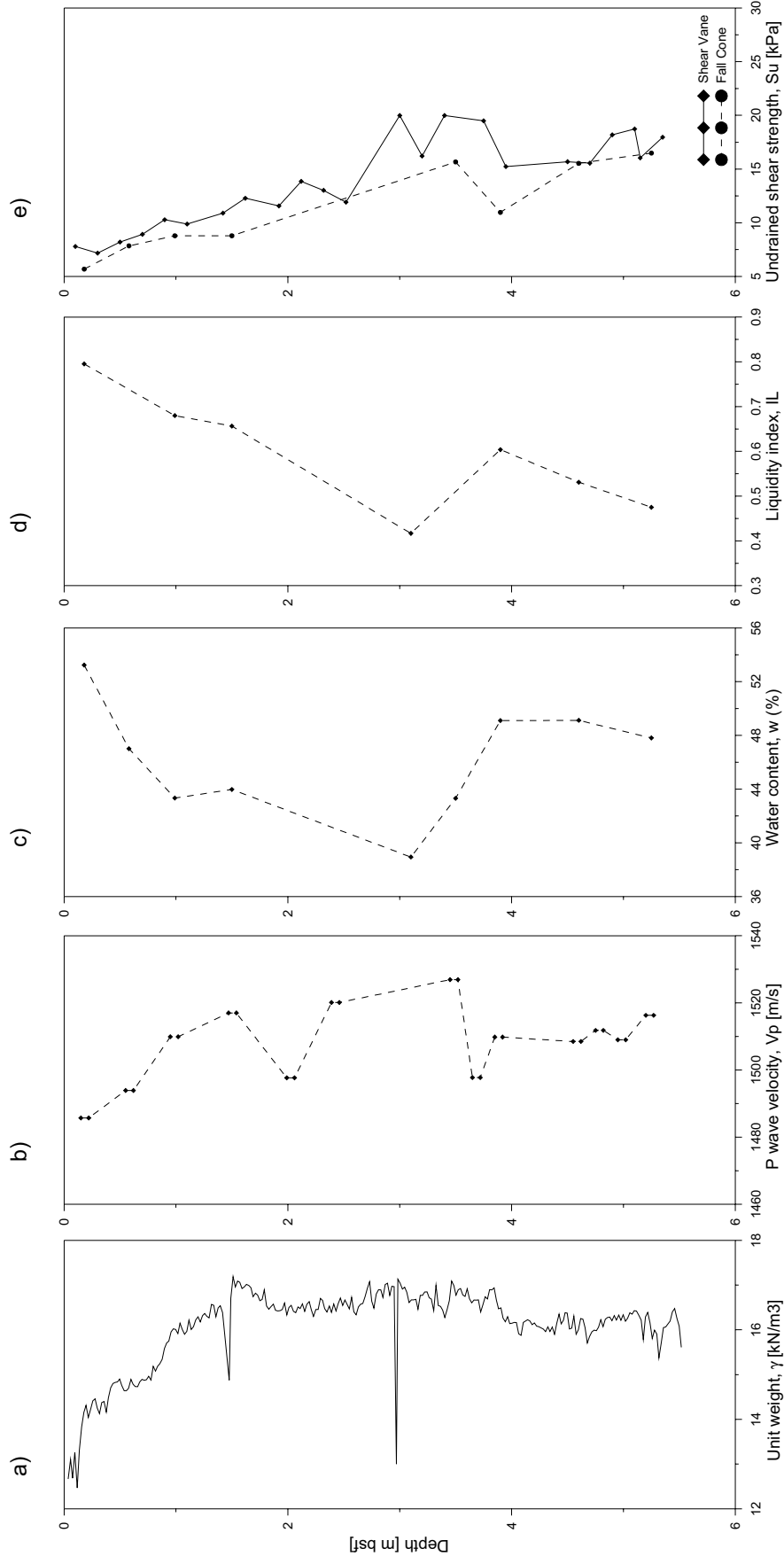


Figure 9.

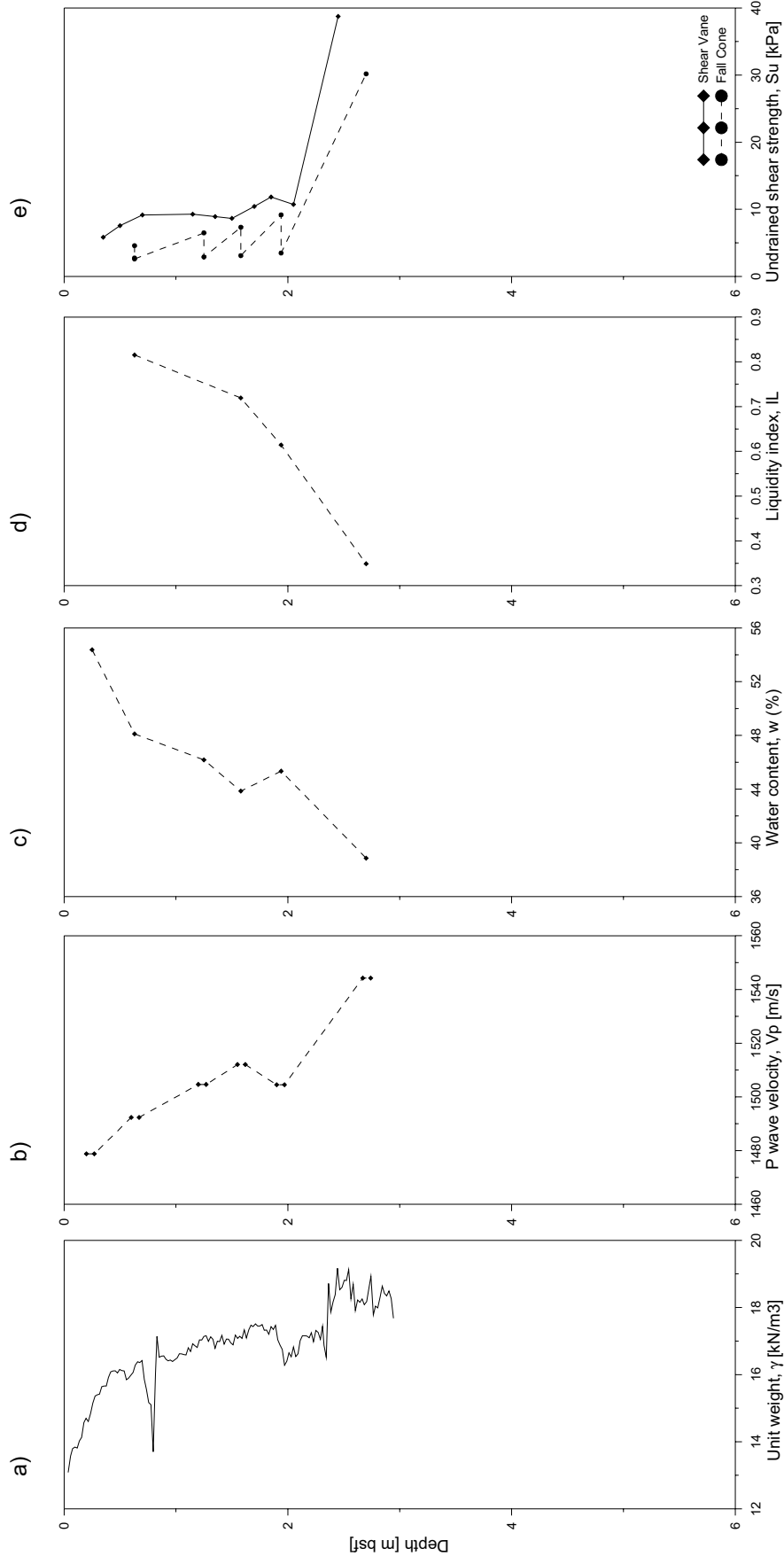
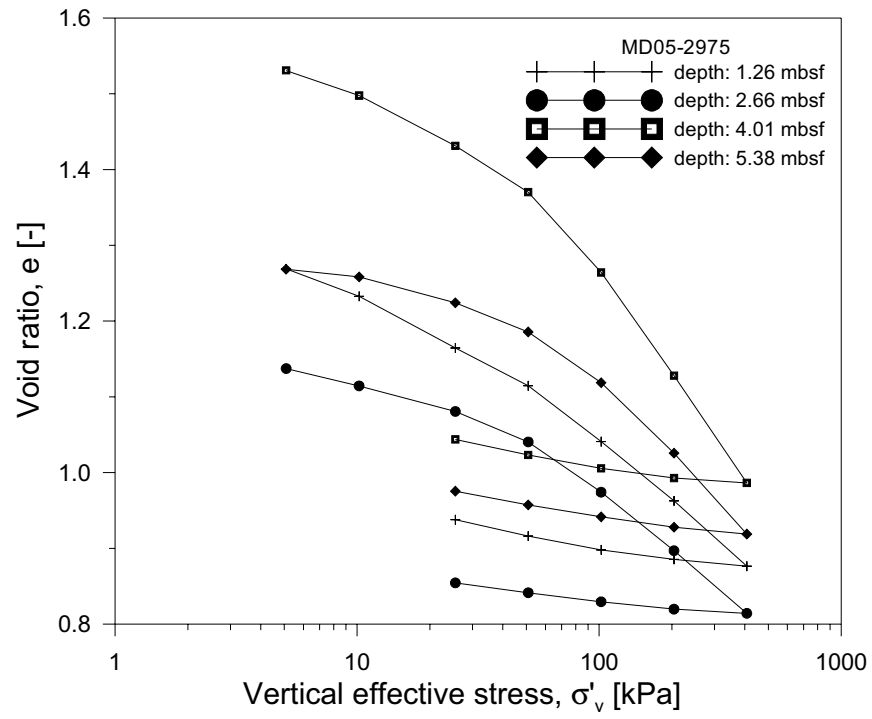


Figure 10.

a)



b)

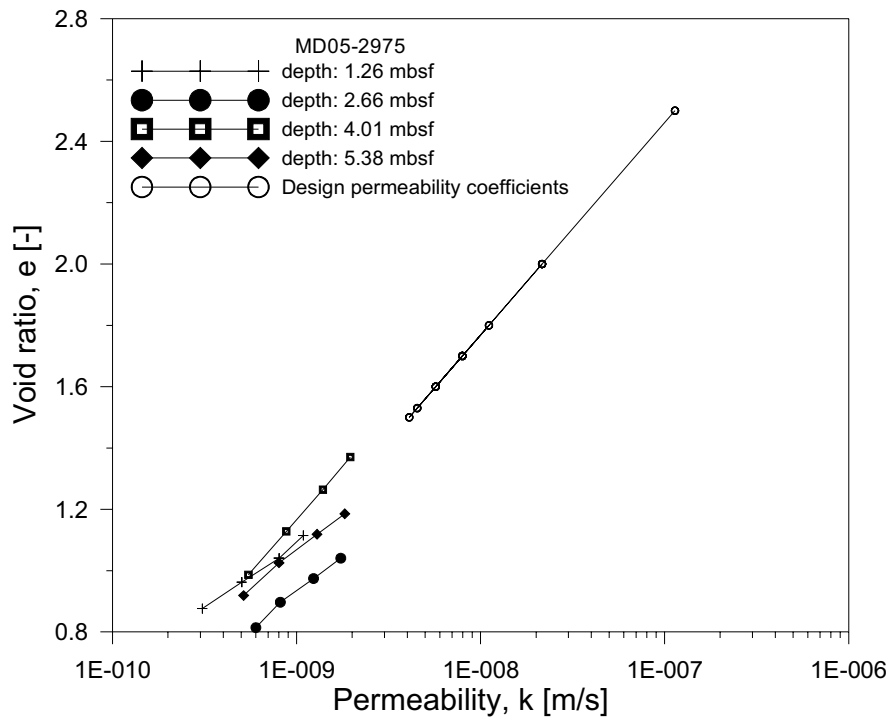


Figure 11.

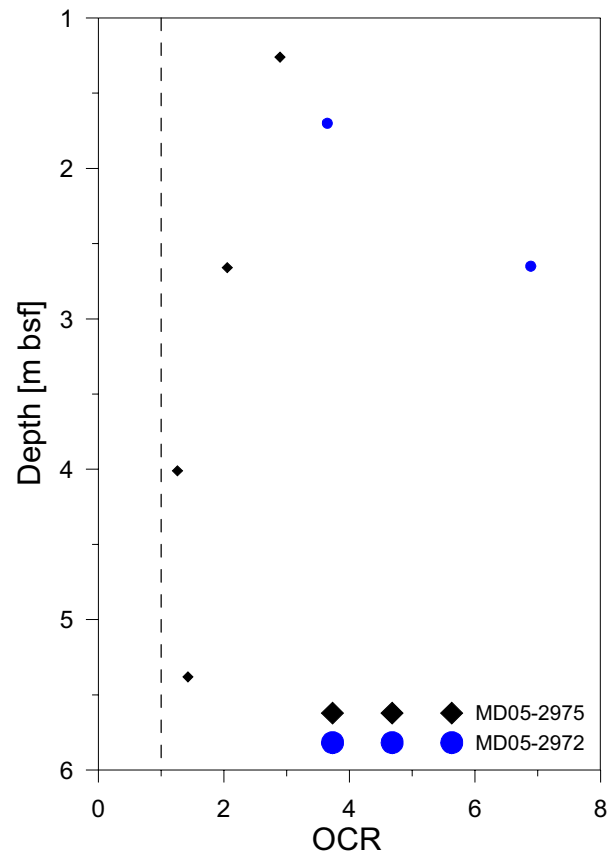


Figure 12.

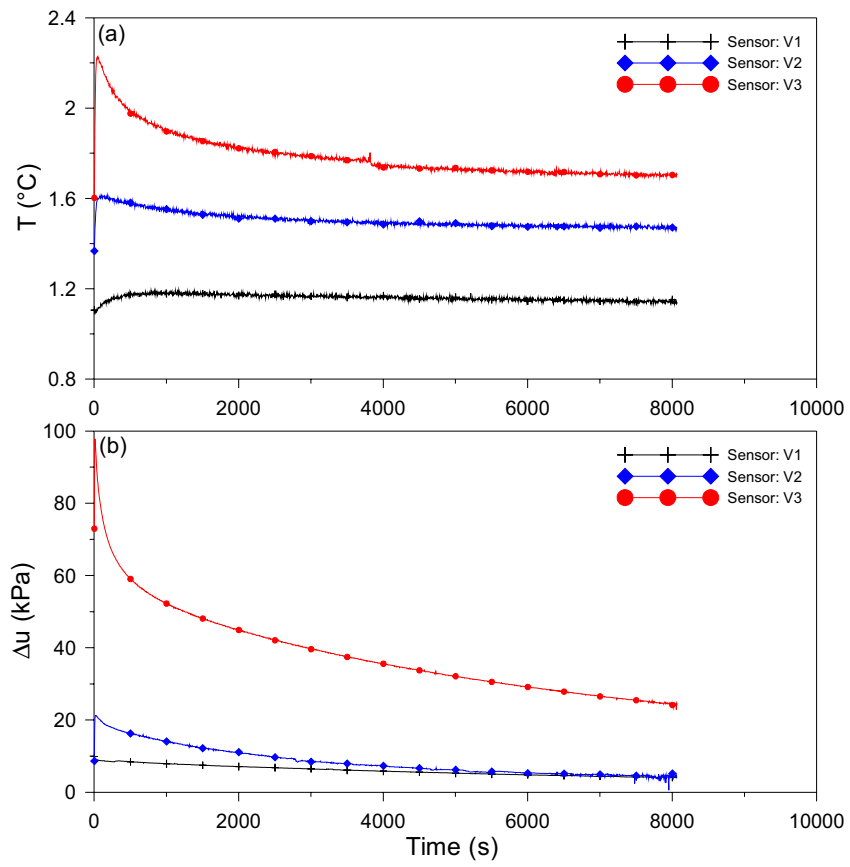


Figure 13.

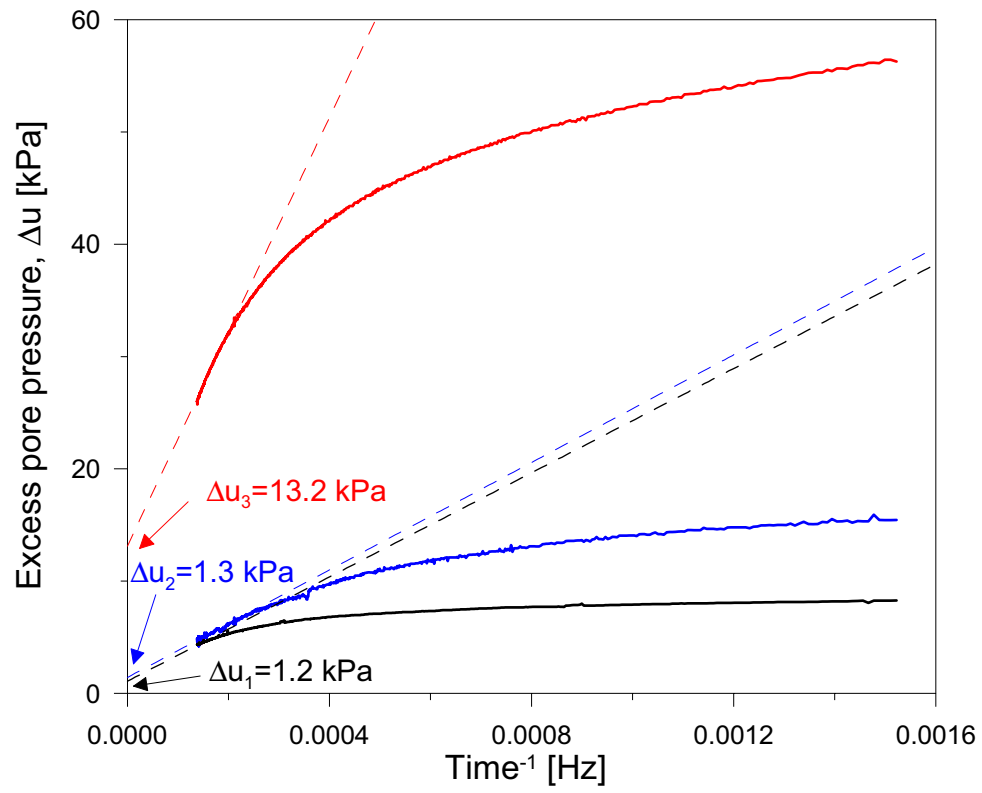


Figure 14.

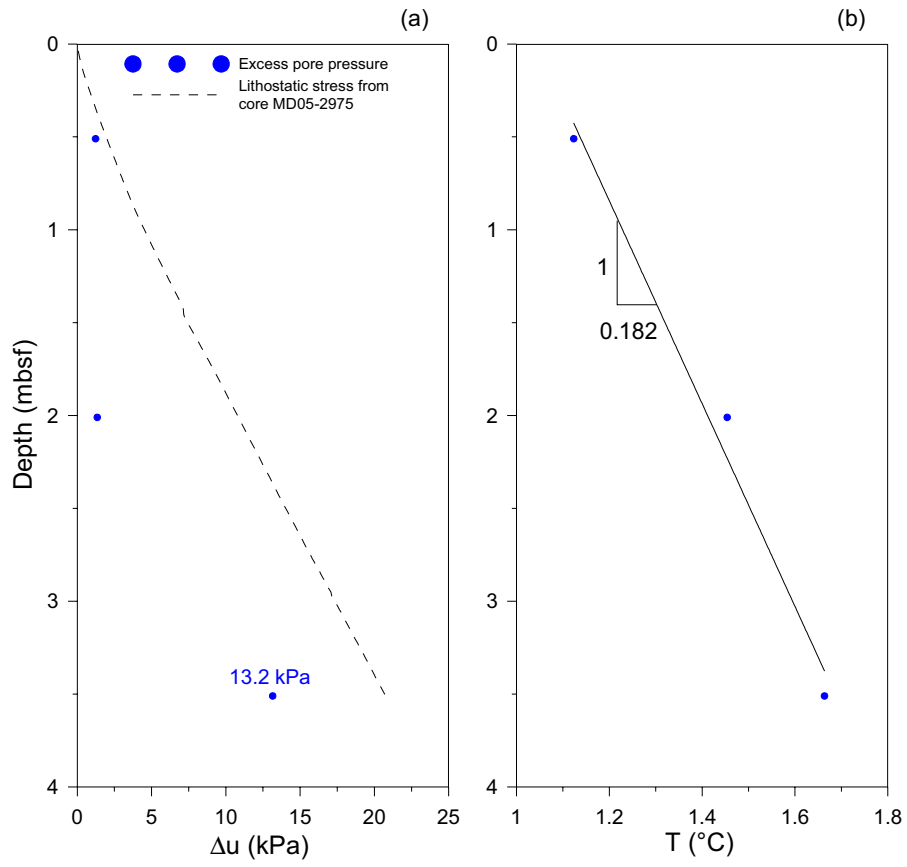


Figure 15.

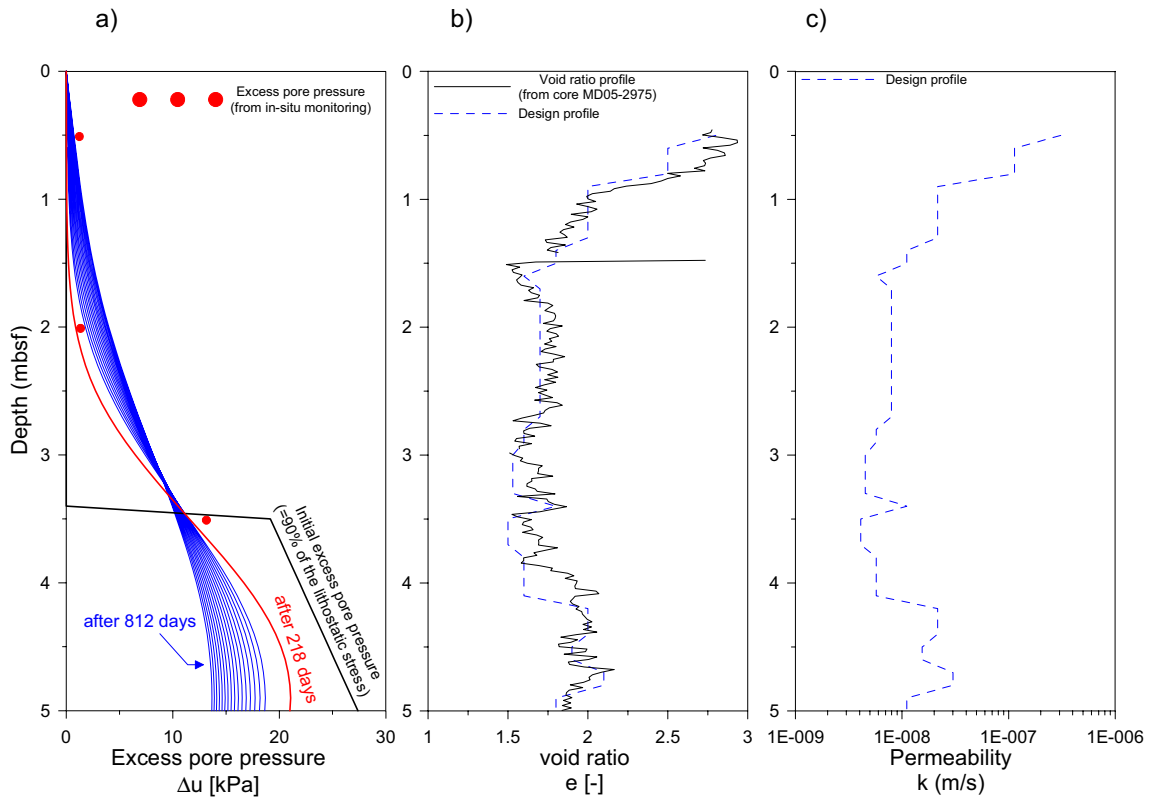


Figure 16.

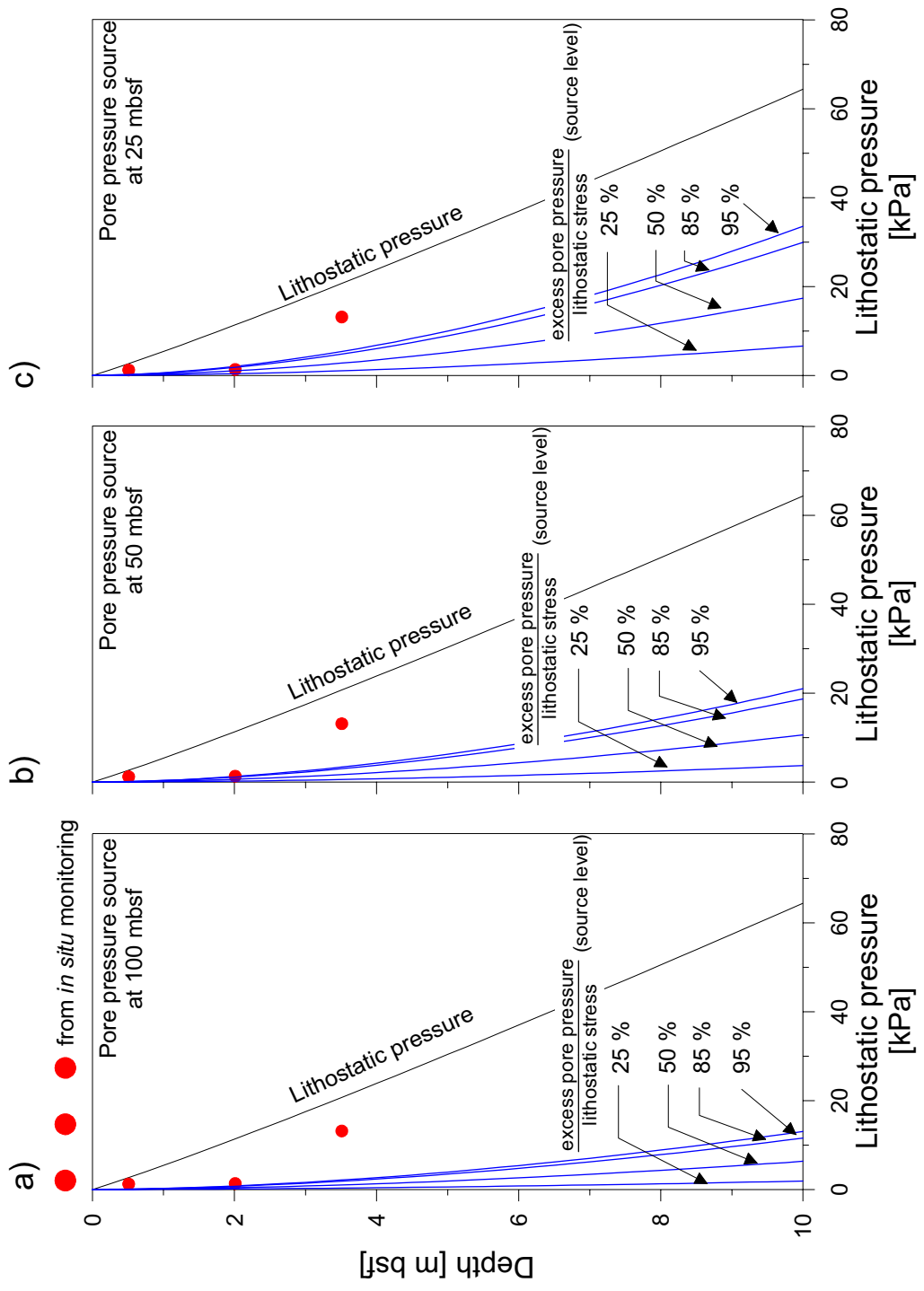


Figure 17.

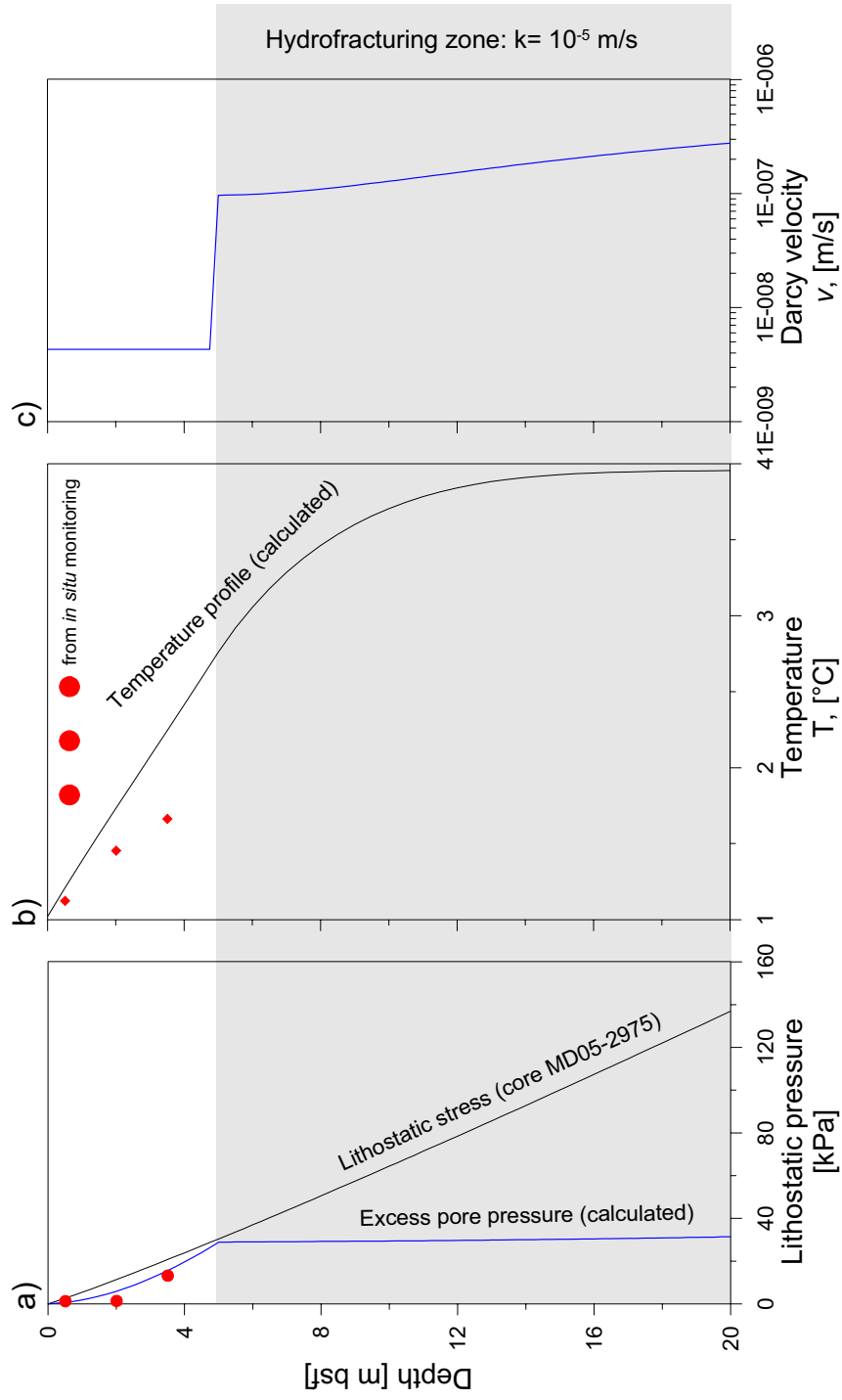


Figure 18.